A&A 654, A22 (2021)
https://doi.org/10.1051/0004-6361/202140981

Astronomy & Astrophysics

Constraining particle acceleration in Sgr A⋆ with simultaneous GRAVITY, *Spitzer*, *NuSTAR*, and *Chandra* observations

GRAVITY Collaboration⋆: R. Abuter[8], A. Amorim[6,12], M. Bauböck[1], F. Baganoff[20], J. P. Berger[5,8], H. Boyce[21,22], H. Bonnet[8], W. Brandner[3], Y. Clénet[2], R. Davies[1], P. T. de Zeeuw[10,1], J. Dexter[14,1], Y. Dallilar[1,⋆⋆], A. Drescher[1,17], A. Eckart[4,18], F. Eisenhauer[1], G. G. Fazio[19], N. M. Förster Schreiber[1], K. Foster[30], C. Gammie[25], P. Garcia[7,12], F. Gao[1], E. Gendron[2], R. Genzel[1,11], G. Ghisellini[13], S. Gillessen[1], M. A. Gurwell[19], M. Habibi[1], D. Haggard[21,22], C. Hailey[27], F. A. Harrison[30], X. Haubois[9], G. Heißel[2], T. Henning[3], S. Hippler[3], J. L. Hora[19], M. Horrobin[4], A. Jiménez-Rosales[1], L. Jochum[9], L. Jocou[5], A. Kaufer[9], P. Kervella[2], S. Lacour[2], V. Lapeyrère[2], J.-B. Le Bouquin[5], P. Léna[2], P. J. Lowrance[23], D. Lutz[1], S. Markoff[26], K. Mori[27], M. R. Morris[24], J. Neilsen[29], M. Nowak[16,2], T. Ott[1], T. Paumard[2], K. Perraut[5], G. Perrin[2], G. Ponti[14,1,⋆⋆], O. Pfuhl[8,1], S. Rabien[1], G. Rodríguez-Coira[2], J. Shangguan[1], T. Shimizu[1], S. Scheithauer[3], H. A. Smith[19], J. Stadler[1], D. K. Stern[31], O. Straub[1], C. Straubmeier[4], E. Sturm[1], L. J. Tacconi[1], F. Vincent[2], S. D. von Fellenberg[1,⋆⋆], I. Waisberg[15,1], F. Widmann[1], E. Wieprecht[1], E. Wiezorrek[1], S. P. Willner[19], G. Witzel[18], J. Woillez[8], S. Yazici[1,4], A. Young[1], S. Zhang[28], and G. Zins[9]

(Affiliations can be found after the references)

Received 1 April 2021 / Accepted 1 July 2021

ABSTRACT

We report the time-resolved spectral analysis of a bright near-infrared and moderate X-ray flare of Sgr A⋆. We obtained light curves in the M, K, and H bands in the mid- and near-infrared and in the 2−8 keV and 2−70 keV bands in the X-ray. The observed spectral slope in the near-infrared band is $\nu L_\nu \propto \nu^{0.5\pm0.2}$; the spectral slope observed in the X-ray band is $\nu L_\nu \propto \nu^{-0.7\pm0.5}$. Using a fast numerical implementation of a synchrotron sphere with a constant radius, magnetic field, and electron density (i.e., a one-zone model), we tested various synchrotron and synchrotron self-Compton scenarios. The observed near-infrared brightness and X-ray faintness, together with the observed spectral slopes, pose challenges for all models explored. We rule out a scenario in which the near-infrared emission is synchrotron emission and the X-ray emission is synchrotron self-Compton. Two realizations of the one-zone model can explain the observed flare and its temporal correlation: one-zone model in which the near-infrared and X-ray luminosity are produced by synchrotron self-Compton and a model in which the luminosity stems from a cooled synchrotron spectrum. Both models can describe the mean spectral energy distribution (SED) and temporal evolution similarly well. In order to describe the mean SED, both models require specific values of the maximum Lorentz factor $\gamma_{\rm max}$, which differ by roughly two orders of magnitude. The synchrotron self-Compton model suggests that electrons are accelerated to $\gamma_{\rm max} \sim 500$, while cooled synchrotron model requires acceleration up to $\gamma_{\rm max} \sim 5 \times 10^4$. The synchrotron self-Compton scenario requires electron densities of $10^{10}\,{\rm cm}^{-3}$ that are much larger than typical ambient densities in the accretion flow. Furthermore, it requires a variation of the particle density that is inconsistent with the average mass-flow rate inferred from polarization measurements and can therefore only be realized in an extraordinary accretion event. In contrast, assuming a source size of $1\,R_{\rm S}$, the cooled synchrotron scenario can be realized with densities and magnetic fields comparable with the ambient accretion flow. For both models, the temporal evolution is regulated through the maximum acceleration factor $\gamma_{\rm max}$, implying that sustained particle acceleration is required to explain at least a part of the temporal evolution of the flare.

Key words. Galaxy: center – accretion, accretion disks – black hole physics

1. Introduction

It is believed that most galaxies harbor at least one supermassive black hole (BH) at their center (Kormendy & Ho 2013). However, only a small fraction are accreting at a high rate and appear as active galactic nuclei. The vast majority are quiescent and therefore inaccessible to us. One exception is Sgr A⋆. Located only 8.27 kpc from us (GRAVITY Collaboration 2019, 2021; Do et al. 2019), Sgr A⋆ is the closest supermassive BH, and has a mass of $(4.297 \pm 0.013)\,M_\odot$ and a corresponding Schwarzschild radius of $R_{\rm S} = 2GM_{\rm BH}/c^2 \sim 1.3 \times 10^{10}$ m. Because it is so close, Sgr A⋆ appears orders of magnitudes brighter than any other supermassive BH in quiescence despite its faint X-ray flux of $\sim 2 \times 10^{33}\,{\rm erg\,s^{-1}}$ (Baganoff et al. 2003). Therefore, Sgr A⋆ offers a unique opportunity to study the physics of accretion in quiescent systems.

The majority of the steady radiation from Sgr A⋆ is emitted at submillimeter frequencies. This radiation is most likely produced by optically thick synchrotron emission originating from relativistic thermal electrons in the central ∼10 Schwarzschild radii ($R_{\rm S}$) at temperatures of $T_{\rm e} \sim$ a few 10^{11} K and densities $n_{\rm e} \sim 10^7\,{\rm cm}^{-3}$, embedded in a magnetic field with a strength of

⋆ GRAVITY is developed in a Collaboration by the Max Planck Institute for extraterrestrial Physics, LESIA of Observatoire de Paris/Université PSL/CNRS/Sorbonne Université/Université de Paris and IPAG of Université Grenoble Alpes/CNRS, the Max Planck Institute for Astronomy, the University of Cologne, the CENTRA – Centro de Astrofisica e Gravitação, and the European Southern Observatory.

⋆⋆ Corresponding authors; S. D. von Fellenberg (e-mail: sefe@mpe.mpg.de), G. Ponti (e-mail: ponti@mpe.mpg.de), and Y. Dallilar (e-mail: ydalillar@mpe.mpg.de).

~10−50 G (Loeb & Waxman 2007; von Fellenberg et al. 2018; Bower et al. 2019). This implies that the accretion flow at a few Schwarzschild radii from the BH is strongly magnetized. For an ambient magnetic field strength of $B \sim 40$ G and ambient $n_e \sim 10^6$ cm^{-3}, we estimate a plasma parameter β of ~0.04 (comparing the thermal pressure of the gas with the magnetic pressure), and $\sigma_{th} \sim 15$ (comparing the magnetic field energy with the thermal energy).

In the X-ray band, Sgr A* appears as a faint ($L_{2-10\,keV} \sim 2 \times 10^{33}$ erg s^{-1}) extended source with a size, $\sim 1''$, comparable to the Bondi radius, emitting via bremsstrahlung emission from a hot plasma with $T_e \sim 7 \times 10^7$ K and $n_e \sim 100$ cm^{-3} (Quataert 2002; Baganoff et al. 2003; Xu et al. 2006). In the X-ray band, Sgr A* occasionally shows sudden rises (flares) of up to 1−2 orders of magnitudes, suggesting individual and distinct events, randomly punctuating an otherwise quiescent source (Baganoff et al. 2001; Porquet et al. 2003, 2008; Neilsen et al. 2013; Ponti et al. 2015; Bouffard et al. 2019). X-ray flares are associated with bright flux excursions in the near-infrared (NIR) band, which also led to the definition of the latter as flares (Genzel et al. 2003; Ghez et al. 2004). However, the IR emission is continuously varying (Do et al. 2009; Meyer et al. 2009; Witzel et al. 2018).

In 2018, GRAVITY Collaboration (2018) reported the first detection of an orbital signature in the centroid motion of three Sgr A* flares. The centroid motion of the three flares is consistent with a source on a relativistic orbit around the BH. Using a fully general relativistic model of a "hot spot", the authors derived a typical orbital radius of around ~4.5 R_S, constrained the emission regions to ~2.5 R_S, and a viewing angle of $i \sim 140$ deg (the inclination of the orbital plane to the line of sight). This model was extended by GRAVITY Collaboration (2020a), who showed that the flare light curves may be modulated by Doppler boosting on the order a few tens of percent. The polarimetric analysis of these flares showed consistent results (GRAVITY Collaboration 2020b). These findings further cement the picture of flares originating from localized regions of the accretion flow in which particles are heated or accelerated.

However, the radiative mechanism powering flares is still disputed. The most common proposed mechanisms are as follows: synchrotron with a cooling break, synchrotron self-Compton (SSC), inverse Compton (IC), and synchrotron (Markoff et al. 2001; Yuan et al. 2003; Eckart et al. 2004, 2006, 2008, 2009, 2012; Yusef-Zadeh et al. 2006, 2008, 2009; Hornstein et al. 2007; Marrone et al. 2008; Dodds-Eden et al. 2009, 2010; Trap et al. 2011; Dibi et al. 2014; Barrière et al. 2014). Simultaneous determination during an X-ray flare of the photon index (Γ) in the NIR (Γ_{IR}) and X-ray (Γ_X) bands allows us to discriminate synchrotron and synchrotron with a cooling break from the other radiative mechanisms. It is expected that $\Gamma_X = \Gamma_{IR}$ or $\Gamma_X = \Gamma_{IR} + 0.5$ for the synchrotron and synchrotron with a cooling break model, respectively (Kardashev 1962; Pacholczyk 1970; Dodds-Eden et al. 2010; Ponti et al. 2017). Any other value would favor either SSC or IC scenarios.

Thanks to an extensive multiwavelength monitoring campaign covering from the IR (with SINFONI) to X-ray (with *XMM-Newton+NuSTAR*), Ponti et al. (2017) observed a very bright NIR and X-ray flare in August 2014. The radiative mechanism was consistent with synchrotron emission all the way from IR to X-ray, therefore implying the presence of a powerful accelerator (with $\gamma_{max} > 10^{5-6}$) and an evolving cooling break and high-energy cutoff in the distribution of accelerated particles. This demonstrated that, at least for that flare, synchrotron emission with a cooling break and a varying high-energy cutoff is a viable mechanism.

To obtain a better insight into the flaring activity of Sgr A*, we deployed a large multiwavelength campaign in July 2019. The campaign was built around a core of three strictly simultaneous 16 h *Chandra* and *Spitzer* observations covering emission from Sgr A* in the soft X-ray and *M* band (PI G.G. Fazio). In addition, two long *NuSTAR* exposures were performed to simultaneously cover the entire campaign in the hard X-ray band. Finally, a ~6.5 h observation with the VLTI-GRAVITY interferometer was performed in the night between July 17 and 18, expanding the campaign to the *K* and *H* bands. For simplicity, we refer to the IR observations by the observing band most similar with the effective wavelength of the observations throughout the paper. Table 1 reports the effective wavelength. Observations with the Submillimeter Array (Witzel et al. 2021) were approved but not executed, owing to a number of factors including weather and limited access to the array during the summer of 2019. During the time window when all instruments were active, we caught a bright IR and moderate X-ray flare. We report in this work the characterization and evolution of the IR to X-ray spectral energy distribution (SED) during the flare and the implications for our understanding of particle acceleration during the Sgr A* flares.

2. Data reduction

2.1. Basic assumptions

Throughout this paper we assume a distance to Sgr A* of 8.249 kpc and a mass $M_{BH} = 4.26 \times 10^6\,M_\odot$ (GRAVITY Collaboration 2020a,b,c). The quoted errors and upper limits are at the 1σ and 90% confidence level, respectively. The X-ray data were initially fitted with XSPEC v. 12.10.1f, employing the Cash statistics in spectral fits (Cash 1979). Throughout our analysis and discussion we make the following assumptions:

- Effects of beaming are negligible.
- Emission is dominated by a single emitting zone.
- Unless otherwise stated, we follow Do et al. (2009) and assume a constant escape time of the synchrotron emitting electrons equal to $t_{esc} = 120$ s.

2.2. Chandra

A series of three *Chandra* (Weisskopf et al. 2000) observations was analyzed (see Table 1). To enhance sensitivity and reduce the effects of pile-up during flares of Sgr A*, the observations were taken with ACIS-S at the focus (Garmire et al. 2006). Only one CCD was active (S3) with a one-eighth subarray (i.e., 128 rows) and no grating applied. The data were reduced with standard tools from the CIAO analysis suite, version 4.12 (Fruscione et al. 2006) and calibration database v4.9.3, released on October 16, 2020. The data from each observation were reprocessed applying the CHANDRA_REPRO script with standard settings. Barycentric corrections with the task AXBARY were applied to the events files, the aspect solution, and all products. To match the exposure of the GRAVITY light curves, we computed light curves in the 2−8 keV, 2−4 keV, and 4−8 keV bands with 380 s time bins, following the GRAVITY exposure time of 320 s plus a dead time of approximately 60 s. Considering the small number of events during quiescence, we represent the count rates following the Gehrels approximation ($\sqrt{(N + 0.75)} + 1$; Gehrels 1986).

During OBSID 22230, we observed a peak count rate of 0.09 ph s^{-1} in the 2−8 keV band. Given the instrumental setup, pile-up effects are negligible even at the peak (e.g.,

Table 1. Datasets analyzed in this work.

Instrument	OBSID	Start (UTC)	Start (MJD)	Exp (ks)	Energy	Wavelength
Chandra	22230	2019-07-17 22:51:26	58681.9524	57.6	2–8 keV	6.2–1.6 Å
	20446	2019-07-21 00:00:14	58685.0002	57.6	2–8 keV	6.2–1.6 Å
	20447	2019-07-26 01:32:40	58690.0639	57.6	2–8 keV	6.2–1.6 Å
NuSTAR	30502006002	2019-07-17 21:51:09	58681.9105	38.6	2–70 keV	6.2–0.2 Å
	30502006004	2019-07-26 00:41:09	58690.0286	34.8	2–70 keV	6.2–0.2 Å
GRAVITY	0103.B-0032(D)	2019-07-17 23:32:55	58681.9812	21.6	0.7–0.8 eV	2.2–1.65 μm
Spitzer	69965312	2019-07-17 23:21:33	58681.9733	17.6	0.3 eV	4.5 μm
	69965568	2019-07-18 07:25:02	58682.3091	17.6	0.3 eV	4.5 μm

Notes. The table reports the instrument used, the identification number of the dataset, the start time of the observation, the total exposure, energy bands, and effective wavelengths of the different instruments.

Ponti et al. 2015). By using the Ponti et al. (2015) conversion factors, we estimate a total observed (absorbed) energy of $\sim 3.2 \times 10^9$ erg released during the flare in the 2−8 keV band. Following the classification of Ponti et al. (2015), this flare belongs to the group of moderate flares in the X-ray band.

Photons from Sgr A* were extracted from a circular region of 1.25″ radius. The spectrum of the flare was extracted with SPECEXTRACT within the time interval MJD = 58682.134:58682.148 (see dotted lines in Fig. 2) and contains a total of 72 photons in the 2−10 keV band. The background spectrum was extracted from the same source region but from the events file accumulated during OBSID 20447, during which no flare of Sgr A* was detected.

2.3. NuSTAR

To study the flare characteristics in the hard X-ray band, we analyzed the two *NuSTAR* (Harrison et al. 2013) observations taken in July 2019 in coordination with GRAVITY, *Chandra*, and *Spitzer* (Table 1). We processed the data using the *NuSTAR* Data Analysis Software NUSTARDAS and HEASOFT v. 6.28, and CALDB v20200912, filtered for periods of high instrumental background due to South Atlantic Anomaly passages and known bad detector pixels. The data were barycenter corrected. Products were extracted from a region of radius 20″ centered on the position of Sgr A* using the tool NUPRODUCTS within the intervals shown in Fig. 2. The background spectra were extracted from the same region in the off-flare intervals within the same observation. In particular, the background spectrum was integrated for each orbit during which no X-ray flares nor bright IR flux excursions were observed in the *NuSTAR* and *Chandra* as well as the GRAVITY and *Spitzer* light curves (Boyce et al., in prep.), resulting in a net exposure time of ∼30 ks. Because part of the FPMB instrument is affected by stray light as a result of a Galactic Center X-ray transient outside of the field of view, we only present the analysis of the FPMA data. The results from FPMB are consistent with those presented in this work. The light curves were accumulated in the 3−10 keV band and with 380 s time bins for comparison with the GRAVITY data. Bins with small fractional exposures were removed.

2.4. Spitzer/IRAC

The observations were obtained using the IRAC instrument (Fazio et al. 2004) on the *Spitzer* Space Telescope (Werner et al. 2004). The observations were part of the *Spitzer* program 14026 (Fazio et al. 2018), which observed Sgr A* at 4.5 μm during three epochs of ∼16 h each in 2019 July. The observing sequence included an initial mapping operation and then two successive eight-hour staring-mode observations, each using the "PCRS peak-up" to center Sgr A* on pixel (16,16) of the subarray. We used a similar data pipeline as described by Hora et al. (2014), Witzel et al. (2018), and Boyce et al. (2019) to derive differential flux measurements. Modifications to the procedure for reduction and calibration of the light curves were necessary because of the larger pointing drift compared to previous observations (about one full pixel over the first three hours of the staring observation). The procedure was modified to transition to the neighboring pixel for the flux measurement when the drift moved Sgr A* into that pixel, roughly one hour after the start of the stare. Also because of the large drift, we derived a new calibration curve that would be valid over the larger range. We used observations of standard stars previously obtained for the subarray "sweet spot" calibration (Ingalls et al. 2012), and found that a fifth-degree polynomial using the distance from the center of the pixel and central pixel flux density provided an acceptable fit to the total flux density of a point source with a standard deviation consistent with the signal-to-noise ratio (S/N) of the observations.

The uncertainty of the *Spitzer* light curve was estimated by computing the standard deviation of the light curve sections where the GRAVITY K-band flux was low. Because the light curve shows residual artifacts from the imperfect background subtraction, we scaled the standard deviation such that low-flux parts of the light curve have $\chi^2_{\rm red} = 1$ with respect to zero mean flux. The flux was de-reddened using the Fritz et al. (2011) extinction values reported in Table 2. Because the *Spitzer* light curve was derived through differential photometry, we needed to add a flux offset. We used the method described by Witzel et al. (2018) to account for the flux offset but used the median K-band flux derived by GRAVITY Collaboration (2020c). Explicitly, we added 1.8 ± 0.3 mJy to all differential flux measurements of *Spitzer*.

2.5. GRAVITY

The interferometric K-band flux density was determined in the same way as by GRAVITY Collaboration (2020c). The values reported are the coherent flux values corrected for the contribution of the star S2. We neglected the contribution of the star S62, which amounts to a constant flux of ∼0.1 mJy. For the details of the flux determination, see GRAVITY Collaboration (2020c).

Table 2. Extinction values of Fritz et al. (2011) in magnitudes.

Band	Fritz et al. (2011)
A_H	4.21 ± 0.08
A_{Ks}	2.42 ± 0.002
A_M	0.97 ± 0.03

Notes. The uncertainties of Fritz et al. (2011) have been propagated only taking the uncertainty of the spectral slope into account.

The H-band flux was determined from aperture photometry of the deconvolved acquisition camera images. The acquisition camera of GRAVITY is normally used for the acquisition of the observation as well as the field and pupil tracking for each of the four unit telescopes. In order to use the aquistion camera images for science, we averaged the four images[1]. The images were bad-pixel-corrected and dark-subtracted. We approximated the point spread function (PSF) of the images by a Gaussian. The parameters of the Gaussian were determined by fitting a Gaussian model to the bright star S10, and we used this PSF model to deconvolve the images using the Lucy-Richardson algorithm implemented in dpuser[2].

In the K and H bands we measured the flux ratio of Sgr A* relative to S2. Because Sgr A* is a much redder source than S2 (Genzel et al. 2010), we had to take the difference in spectral index into account. For the K band this was achieved by fitting a power-law spectrum to both sources and determining the flux at 2.2 µm. For the H band, we accounted for this difference in spectral index by assuming that the reddened flux from both sources is described by a power law. We used NACO photometry of S2 to determine the reddened spectral slope of S2. By using the observed flux ratio in the H and K bands and the transmission curve of the acquisition camera detector, we derived the effective wavelength of Sgr A* in the H band: $\lambda_{\mathrm{Sgr\ A*}} \sim 1.63$ µm. Once the effective wavelength was determined, we used the observed flux ratio in the H and K band to determine the flux density of Sgr A* in the H band. The details of this are outlined in Appendix B.

2.6. Extinctionx

The Galactic Center is a highly extincted region, which has an approximately broken-power-law extinction $A(\lambda)$ between 1.2 µm and 8 µm (Fritz et al. 2011). The extinction is a major source of uncertainty for our analysis because even a small variation in the power-law extinction slope leads to a large change in our measured IR spectral slope. The hydrogen column density is similarly a key ingredient in the derivation of the X-ray absorption and thus the modeling of the X-ray spectral slope. Moreover, the hydrogen column density and the IR extinction are related but independently determined. This may therefore lead to a systematic offset between NIR and X-ray observations.

2.6.1. Infrared extinction

We used the extinction model from Fritz et al. (2011), who used the hydrogen emission lines observed with SINFONI at the VLT to derive a broken-power-law extinction curve. This allows us to drop the uncertainty on the absolute calibration and only propagate the uncertainty on the power law exponents. The authors also provided extinction values for NACO and *Spitzer*, tabulated in Table 2. We neglected the uncertainty owing to the difference in filter response between NACO and the two GRAVITY bands.

2.6.2. X-ray extinction

The observed X-ray spectrum is distorted by the combination of absorption and dust scattering. The latter effect produces a halo of emission, which is typically partially included within the limited extraction region used to compute the spectrum of Sgr A*. We fitted the scattering halo of the dust with the model FGCDUST in XSPEC (Jin et al. 2017, 2018), and it was assumed to be the same as the foreground component along the line of sight toward AX J1745.6–2901 (Jin et al. 2017, 2018).

We fit the absorption affecting the X-ray spectra with the model TBABS (see Wilms et al. 2000) with the cross sections of Verner et al. (1996) and abundances from Wilms et al. (2000). Figure 5 shows the impact of the different assumptions for the column density on the X-ray spectral slope. As Ponti et al. (2017), we assumed a column density of $N_{\mathrm{H}} = 1.6 \times 10^{23}$ cm^{-2}.

3. Light curves

Figure 1 shows the full duration of the multiwavelength campaign performed on July 17−18, 2019. The *Spitzer* and GRAVITY light curves follow each other very well. The *Spitzer* light curve shows IR flares in excess of 5 mJy. In particular, two $F_M \gtrsim 15$ mJy and $t \gtrsim 30$ min IR flares are observed by *Spitzer* at MJD∼58682.14 and ∼58682.47. However, only the first IR flare has a detectable X-ray counterpart (Fig. 1), which suggests that one or more additional parameters are required to control the X-ray loudness of the IR flares.

Figure 2 shows a zoom-in of the light curves of the bright IR flare with X-ray counterpart detected on July 18, 2019. As discussed by Boyce et al. (in prep.), the flare occurred nearly simultaneously in the two bands, with the X-ray peak occurring at the maximum of the IR emission. The X-ray flare, as observed by *Chandra*, was shorter (∼19 min duration) than its IR counterpart (∼38 min duration). A shorter duration of the X-ray flare has been observed before (e.g., Dodds-Eden et al. 2010, 2011).

At the start of the flare (T1[3] ∼58682.133) emission was observed in the K and M bands (∼5 mJy) with simultaneous H-band emission but no excess above quiescence in the X-ray band. Soon after, the X-ray band rose very rapidly (T2). It then decayed quickly back to quiescence, while the IR flux rose and decayed more gently (Fig. 2). Indeed, when the X-ray emission reached quiescence, the IR flux density was still above ∼8 mJy in every IR band (Fig. 2; T5 and T6).

4. The multiwavelength flare in context

The IR flare reported in this paper is among the brightest ever observed. It is the third brightest flare observed with GRAVITY, although it is significantly shorter than the flares observed in 2019. The left panel of Fig. 3 shows the flux distribution of Sgr A* (GRAVITY Collaboration 2020c) and compares the peak fluxes of three flares possessing an X-ray counterpart. The flare under investigation in this work is almost an order of magnitude fainter and a factor of ∼2−3 shorter than previously analyzed very bright X-ray flares (Dodds-Eden et al. 2009; Ponti et al. 2017). Thanks to the frequent observations of X-ray emission from Sgr A*, more than 100 X-ray flares

[1] The aquisition camera pipeline will be made available under https://github.com/Sebastiano-von-Fellenberg/AquisitionCamera. It has been written by SvF and Giuila Folchi.
[2] https://www.mpe.mpg.de/~ott/dpuser/

[3] T1 stands for the first time interval of the time resolved analysis.

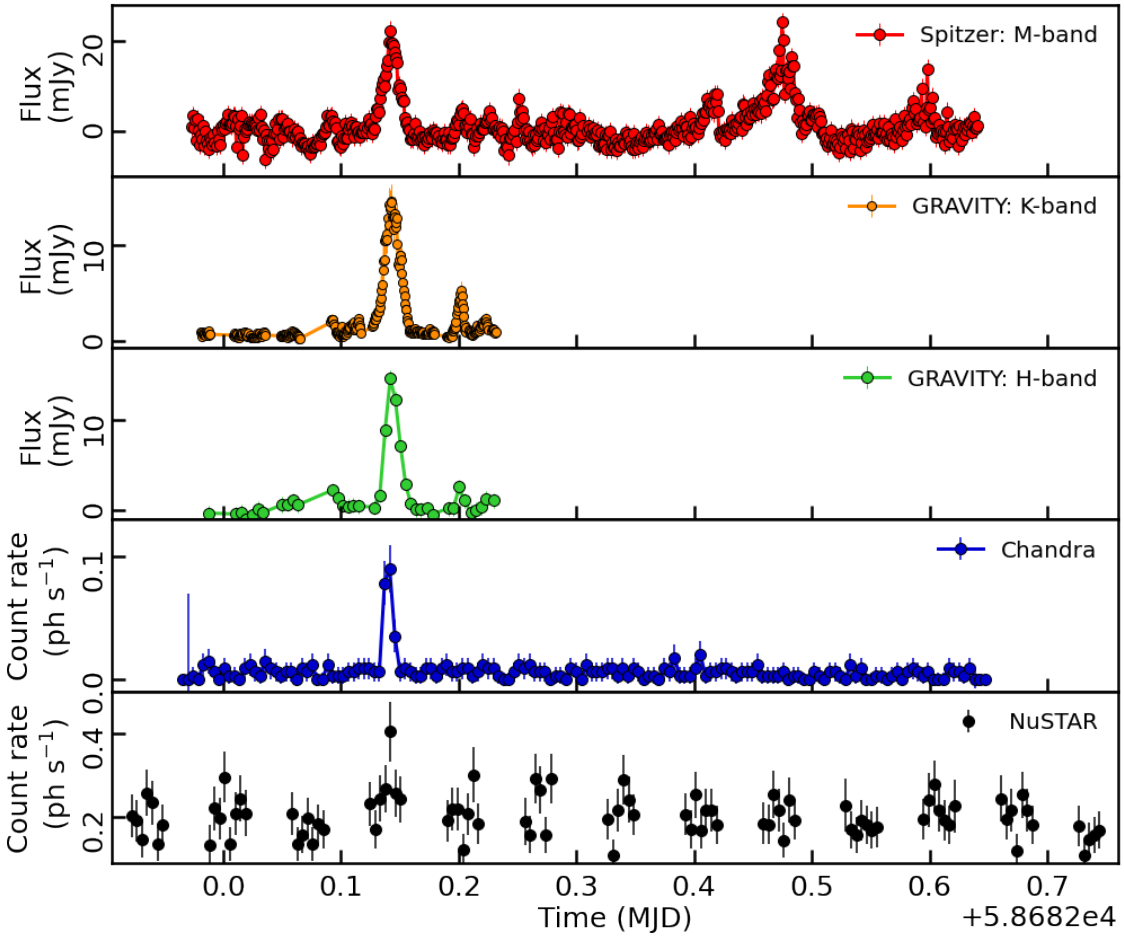

Fig. 1. X-ray and IR light curves of the multiwavelength observations performed on July 18, 2019. The *Spitzer* (red), GRAVITY *K* (orange) and *H* band (green), *Chandra* (blue), and *NuSTAR* (black) data. The *Spitzer* light curves show the differential flux density. The NIR flux densities have been corrected for extinction using the values in Table 2.

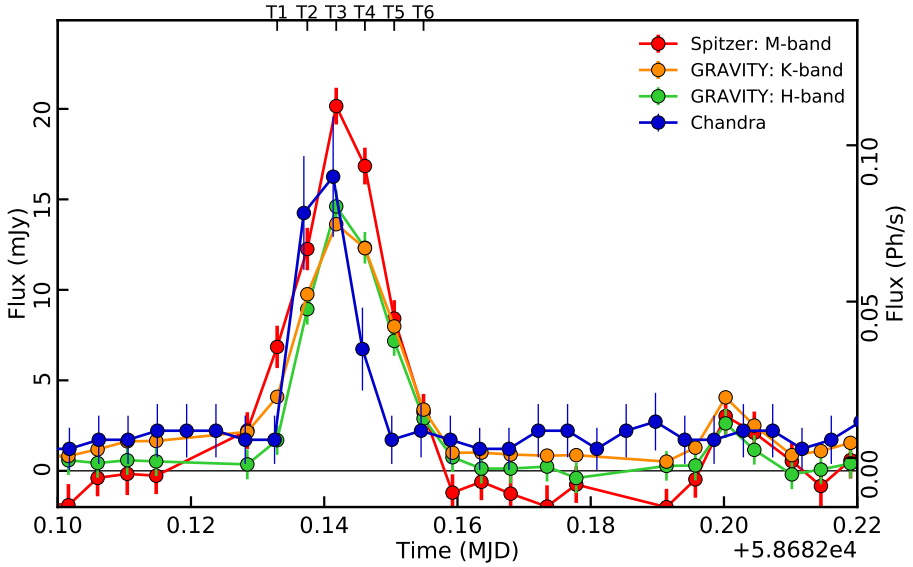

Fig. 2. X-ray and IR light curves of the flare detected on July 18, 2019. The blue points show the *Chandra* light curve in the 2−8 keV band. The red, orange, and green points show *Spitzer* (*M*-band), the GRAVITY *K*-band, and *H*-band light curves corrected for extinction, respectively. The bold ticks on the top abscissa labeled T1, T2, T3, T4, T5, and T6 mark the times that will be used in the subsequent analysis.

of Sgr A* have been detected so far by *Chandra* and *XMM-Newton* (Neilsen et al. 2013; Ponti et al. 2015; Mossoux et al. 2016; Li et al. 2017; Bouffard et al. 2019). Figure 3 highlights the fluence and duration of the X-ray flare detected in this work and compared to previously detected flares.

The July 18 flare shows only moderate emission in the X-ray band. This flare is almost an order of magnitude fainter and a factor of ∼2−3 shorter than the very bright X-ray flares for which the IR to X-ray SED has been investigated in detail in previous works (Dodds-Eden et al. 2009; Ponti et al. 2017). The relative

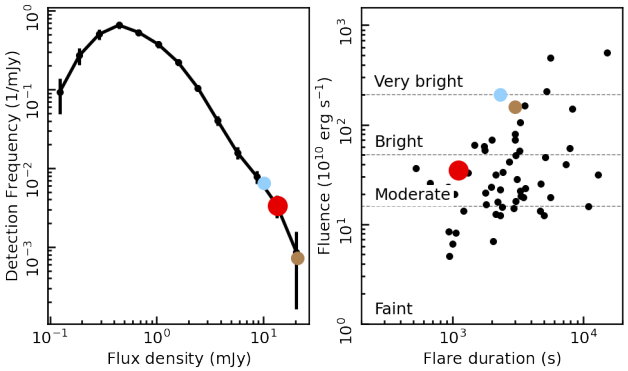

Fig. 3. *Left*: GRAVITY K-band flux density distribution as reported in GRAVITY Collaboration (2020c) and the peak flux densities of three bright flares. The red point indicates the peak flux density of the flare analyzed in this paper. The light blue point indicates the peak flux reported by Ponti et al. (2017) observed with SINFONI. The light brown point represents the peak L'-band flux density scaled to 2.2 µm, assuming a flux density scale $F_{K\,\mathrm{band}} = F_{L'\,\mathrm{band}} \cdot (\nu_K/\nu_{L'})^{-0.5}$. *Right*: duration and fluence of all flares of Sgr A* detected by *XMM-Newton* and *Chandra* before 2015 (see Neilsen et al. 2013; Ponti et al. 2015). Partial (i.e., only partially covered) and dubious flares have been omitted. As in the left plot, the red, light blue, and dark blue circles show the duration and fluence of the X-ray flares investigated in this work, by Ponti et al. (2017), and by Dodds-Eden et al. (2009).

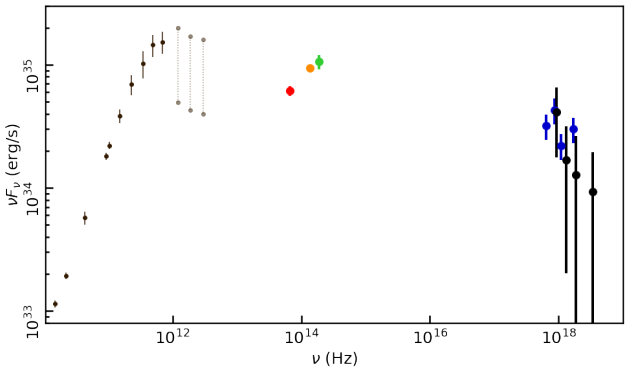

Fig. 4. Mean SED plotted together with the best-fit power-law slope. The submillimeter SED is plotted for orientation; the radio and submillimeter data are from Falcke et al. (1998), Bower et al. (2015, 2019), Brinkerink et al. (2015), Liu et al. (2016). The far-infrared data are from Stone et al. (2016) and von Fellenberg et al. (2018).

X-ray faintness is unexpected, considering that the flare is one of the brightest flares in the IR band.

5. Analysis of the mean spectrum

5.1. Infrared spectrum

To obtain the mean spectrum, we binned all six exposures with significant IR flux to find the average flux density in the M, K, and H bands. These flux densities were converted to luminosities and are shown in Fig. 4.

5.2. Chandra

Dust extinction and absorption due to neutral material along the line of sight are a major source of systematic uncertainty for all observations of the Galactic Center. A fit of the original *Chandra* spectrum with an absorbed power law, corrected for the

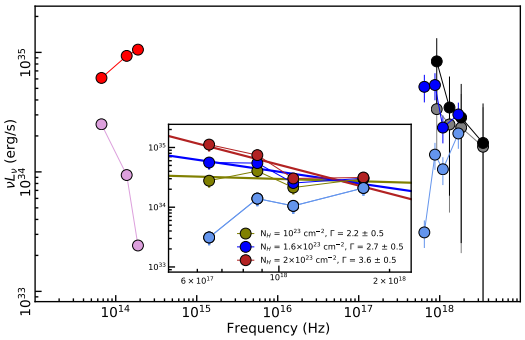

Fig. 5. *Main panel*: comparison between observed and corrected spectra. The cyan, gray, and pink points show the spectra as observed by *Chandra*, *NuSTAR*, and in the IR band, respectively. The blue, black, and red points show the same data corrected for absorption and the effects of dust scattering. The correction amounts to more than one order of magnitude in K and H as well as in the soft X-ray band. *Inset*: as in the main panel, the cyan points show the spectrum as observed by *Chandra*. The olive, blue, and dark red points show the *Chandra* spectrum after correction assuming $N_\mathrm{H} = 10^{23}$, 1.6×10^{23}, and 2×10^{23} cm^{-2}, respectively.

distortions introduced by dust scattering, provides a best-fit photon index $\Gamma = 2.7\pm0.5$ (C-stat = 238.1 for 545 d.o.f.). The best-fit 2–10 keV observed flux is $F_{\mathrm{Abs}\,2-10} = 2.3\times10^{-12}$ erg cm^{-2} s^{-1}. Once de-absorbed and corrected for the effects of dust scattering, this corresponds to $F_{\mathrm{Deabs}\,2-10} = 6.9\times10^{-12}$ erg cm^{-2} s^{-1}. To fit the temporal evolution of the spectrum together with the NIR data, we rebinned the observed spectrum to have four bins in energy each containing 18 photons. For the time-resolved spectra, we binned our spectra in 2, 2, and 1 bins containing 16, 14, and 12 photons for T2, T3, and T4, respectively. Starting from the best-fit model of the original data, we computed the ratio of the absorbed to scattered model and the de-absorbed and dust-scattering-corrected model. We then applied this model ratio to the rebinned spectrum to derive the corrected spectrum of the Sgr A* flare.

The effects of absorption and dust scattering are very significant in the soft X-ray band. A comparison between the observed and de-absorbed spectra shown in Fig. 5 shows a ratio in excess of one order of magnitude below ~3 keV. The soft X-ray flux and X-ray photon index are strongly correlated dependent on the assumed column density of absorbing material (see of Fig. 5). By assuming column densities of $N_\mathrm{H} = 10^{23}$, 1.6×10^{23} and 2×10^{23} cm^{-2} (all values which are consistent with the spectrum of this moderate X-ray flare), the best-fit photon index is $\Gamma = 2.2\pm0.5$, 2.7 ± 0.5, and 3.6 ± 0.5, respectively. These values are consistent with the allowed range of values reported in works compiling several X-ray flares (e.g., Porquet et al. 2008; Nowak et al. 2012). To allow a better comparison with previous multiwavelength flares of Sgr A*, we assume $N_\mathrm{H} = 1.6\times10^{23}$ cm^{-2} (Ponti et al. 2017). We discuss the implications of this choice in Appendix C.

5.3. NuSTAR

As a consequence of the larger PSF of the *NuSTAR* mirrors, a larger fraction of diffuse emission contaminates the *NuSTAR* spectra of Sgr A* compared to *Chandra*. The Sgr A* photons amount to about 30% of the total flux in the 3–20 keV band. We fitted the background spectrum simultaneously with the source plus background to reduce the uncertainties

Table 3. Parameters of the best fit to the *Chandra*, *NuSTAR*, and combined source and background spectra.

X-ray spectral analysis			
	Chandra	*NuSTAR*	*Chandra+ NuSTAR*
Sgr A⋆			
Γ	2.7 ± 0.5	2.6 ± 1.0	2.7 ± 0.5
$N_{\rm pl}$	87^{+90}_{-45}	50^{+300}_{-40}	67^{+90}_{-40}
Background			
$kT_{\rm a}$		1.8 ± 0.2	1.8 ± 0.2
$N_{\rm H}$		2.4 ± 0.4	2.6 ± 0.4
Γ		1.7 ± 0.1	1.7 ± 0.1
$N_{\rm pl}$		12 ± 4	13 ± 4
C-S/d.o.f.	238.1/547	1046.6/1717	1284.6/2264

Notes. The quantity $N_{\rm H}$: the column density of the neutral material (10^{22} atoms cm^{-2}); Γ: the photon index of the power-law component; $N_{\rm pl}$ normalization (10^{-4} photons keV^{-1} cm^{-2} s^{-1} at 1 keV) of the power-law component; $kT_{\rm a}$ plasma temperature (keV) of the APEC component; $N_{\rm a}$ normalization (10^{-2}) of the APEC component; and C-S: value of Cash statistic.

associated with background subtraction, thereby adopting the same background model components in both cases.

We parameterized the *NuSTAR* background spectrum in the 3−50 keV band with a collisionally ionized diffuse plasma component (APEC in XSPEC) plus a power law, all absorbed by neutral material. This model provides a good description of the background spectrum (see Table 3). We simultaneously fitted the source plus background spectrum by adding an absorbed power-law component to this model to fit the emission from Sgr A⋆. The best-fit photon index of Sgr A⋆ emission is $\Gamma = 2.6 \pm 1.0$ with an absorbed 3−20 keV flux of $F_{\rm Abs\,3-20} = 3.1 \times 10^{-12}$ erg cm^{-2} s^{-1} ($F_{\rm Deabs\,3-20} = 4.5 \times 10^{-12}$ erg cm^{-2} s^{-1}).

5.4. Combined fit of Chandra+NuSTAR spectra

Finally, we simultaneously fitted the background subtracted *Chandra* as well as the source plus background and background *NuSTAR* spectra. This provides a good fit to the data, with a best-fit $\Gamma = 2.7 \pm 0.5$ (see Table 3). To perform multiwavelength fits with models not yet implemented in XSPEC (e.g., synchrotron cooling break and high-energy cutoff SSC models), we corrected the binned *Chandra* and the binned[4] background-subtracted *NuSTAR* spectrum for the effects of absorption and dust scattering and then fit the corrected spectrum with a least-squares fit. This step might introduce biases in the corrected spectrum. However, we verified that such distortions are negligible compared to the statistical uncertainties of the X-ray spectra.

6. Temporal evolution of the SED

We can determine a spectral index for each of the six exposures with significant IR flux. In this section, we report the spectral slope of the flux density $F_\nu \propto \nu^\alpha$. The spectral slope of the luminosity is $\nu F_\nu \propto \nu^\beta$, where $\beta = \alpha + 1$. In order to compare the spectrum of the M band to the K band and the K band to the H band, we analytically computed the spectral slope as follows:

$$\alpha_{\rm Band1-Band2} = \log_{(F_{\rm Band1}/F_{\rm Band2})}(\nu_{\rm Band1}/\nu_{\rm Band2}), \quad (1)$$

[4] The *NuSTAR* spectrum has been rebinned to have 21 photons per bin in the 3−40 keV energy band.

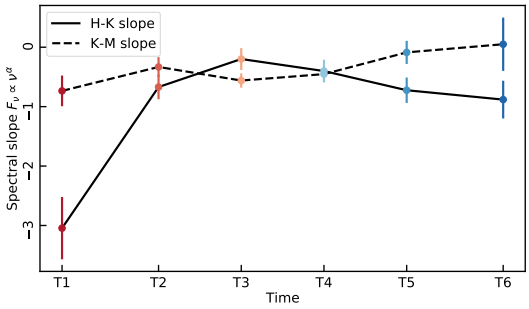

Fig. 6. Infrared spectral slopes α for the six times T1 to T6. The color encodes the time, dark red to dark blue. The black solid line shows the $H-K$ slope; the black dashed line shows the $K-M$ slope.

and we propagated the uncertainty of the observed flux densities (Fig. 6).

During the onset of the flare, Sgr A⋆ was faint in the H band, while there is already substantial flux measured in the M and K bands. This resulted in a very red $H-K$ slope $\sim$−3, while the $K-M$ slope was $\sim$−0.7. After the first data point, the $H-K$ slope jumped to $\sim$−1. For the next two data points, the spectral slope increased from $\alpha_{H-K} \sim -1$ to $\alpha_{H-K} \sim 0$ at the peak of the flare. After the peak α_{H-K} decreased, with $\alpha_{H-K} \sim -1$ at the end of the flare. This indicates a correlation between the $H-K$ spectral slope and the flux density. Conversely, there was no strict correlation of the spectral slope with flux density for α_{H-K}. The $K-M$ slope varied in the range $\alpha_{K-M} = [-0.8, 0.0]$ and increased toward the end of the flare. However, this might be indicative of a correlated error owing to a telescope slew of the *Spitzer* spacecraft. The temporal evolution of the flare SED is shown in Fig. 7.

7. One zone SED model

To model the IR to X-ray SED of Sgr A⋆, we developed a dedicated Python package (Dallilar et al., in prep.). The code implements robust calculation of synchrotron emission or IC scattering from a given underlying electron distribution in a single zone. We also provide a convenient SED fitting interface built on top of the general purpose Python fitting package LMFIT[5]. For testing and convenience, the code includes theoretical solutions to synchrotron emission and absorption coefficients of a thermal, power law, or kappa distribution based on the formalism presented by Pandya et al. (2016). Furthermore, we implemented a fast numerical calculation of the emission and absorption coefficients for a given arbitrary electron distribution. With this feature, we are able to explore more complex electron distributions. This is especially important in the context of including "cooling break" types of models (Dodds-Eden et al. 2009; Ponti et al. 2017) and more realistic cutoff shapes of the electron distribution. Our approach is an improvement compared to similar attempts in the aforementioned works in terms of self-consistent determination of electron distribution parameters from SED fitting. The IC scattering formalism of the code follows the concepts presented by Dodds-Eden et al. (2009). As with synchrotron emission, we can take advantage of arbitrary electron distributions as the scattering medium. Seed photons can be either an external (arbitrary) photon field or synchrotron emission from an underlying electron population, namely, SSC emission. The details of the code will discussed by Dallilar et al. (in prep.).

[5] https://github.com/lmfit/lmfit-py/

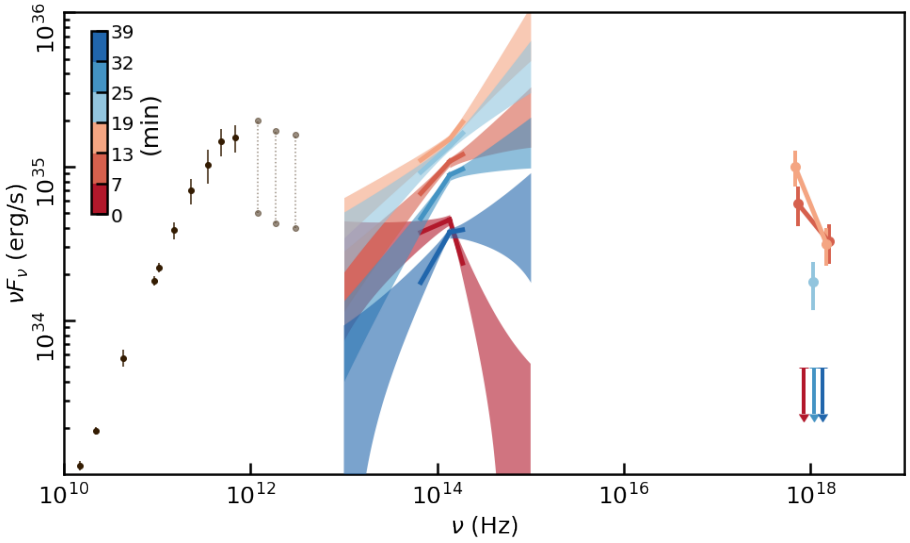

Fig. 7. Temporal evolution of the SED. The color encodes the time: dark red to dark blue as indicated in the color bar. For two time steps, the X-ray spectrum can be split up into two points (T2 and T3). For T4, only one X-ray flux measurement is possible. The upper limits are plotted for T1, T5, and T6. The measurements in the NIR are indicated by thick lines, with the uncertainties indicated and extrapolated by the shaded area. The submillimeter data shown are the same as in Fig. 4.

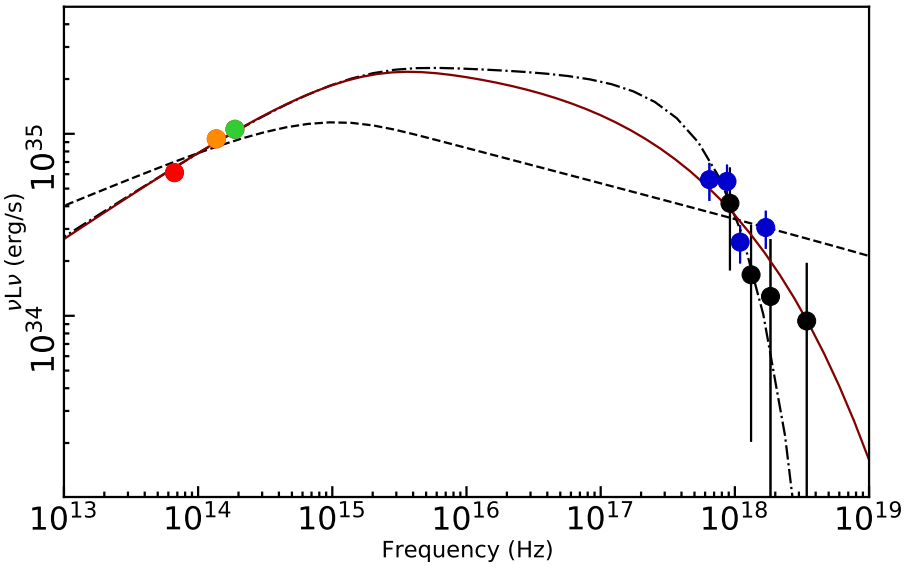

Fig. 8. Mean SED of Sgr A* during the flare as in Fig. 4, including the best-fit synchrotron models. The black dashed line shows the best-fit PLCool model (synchrotron with cooling break model with no high-energy cutoff). This model is ruled out because it cannot fit the difference in X-ray vs. IR spectral slopes due to the X-ray vs. IR flux ratio. The dashed-dotted black lines shows the best fit PLCool$\gamma_{\rm max\,sharp}$ model (synchrotron with cooling break plus a sharp $\gamma_{\rm max}$ cutoff). The line cuts off too sharply in the X-ray and fails to reproduce the high-energy *NuSTAR* data. The dark red line shows the best-fit PLCool$\gamma_{\rm max}$ model (synchrotron with cooling break plus an exponential high energy cutoff). For this model, the SSC component, which peaks at $\nu \sim 10^{23}$ Hz, is also computed (not shown here, see Fig. A.1).

The philosophy of the code is to provide emission scenarios that are as simple as possible. This is achieved by modeling the flares in a scenario in which the emission is dominated by a single localized region in the accretion flow and by a single population of electrons, reducing the number of free parameters. For instance, if the emission is modeled using a power-law distribution of electrons, the number of free parameters is six. Keeping the number of free parameters small is necessary because our limited spectral coverage does not warrant a more complex fit (i.e the number of model parameters should be smaller than the number of observables). Therefore, the luminosity is computed for a homogeneous and spherical geometry of electrons. Ultimately, we can fit the model SED to the data, either through χ^2 minimization or through MCMC modeling.

8. Reproducing the mean SED of the flare

8.1. Synchrotron with a cooling break

We began by fitting the mean spectrum of the flare with a simple synchrotron model with a cooling break (see Fig. 8). We call this model the PLCool model. Although the difference in photon indices between the IR ($\Gamma_{\rm IR} = 1.5 \pm 0.2$) and X-ray ($\Gamma_{\rm X} = 2.7 \pm 0.5$) bands is consistent with the expectations of the synchrotron model with cooling break ($\Delta\Gamma = 0.5$), it is not possible to fit the mean SED of the flare with this model. Indeed, the high luminosity in the IR band combined with the rather flat IR spectrum would imply a very high luminosity in the X-ray band. As a consequence of this tension, the PLCool model settles to a less blue IR slope than observed, failing to satisfactorily fit the data (Fig. 8 and Table 4).

8.2. Synchrotron with a cooling break and sharp high-energy cutoff

The acceleration mechanism generating the flare may not be powerful enough to accelerate particles to $\gamma_{\rm max} \gg 10^5$ at all times (Ponti et al. 2017). If this is true, we expect to observe a high-energy cutoff between the IR and X-ray bands. Hence, we fit the mean SED with a synchrotron model with cooling break and a high-energy cutoff in the electron distribution. We call this model the PLCool$\gamma_{\rm max\,sharp}$. In particular, we assumed that the high-energy cutoff is a step function with no electrons having $\gamma > \gamma_{\rm max}$. We assumed that the electrons are

Table 4. Best-fit parameters of the fit of the SED with the PLCoolgamma model.

	Mean SED			Time resolved					
	PLCool	PLCool$\gamma_{\rm max\,sharp}$	PLCool$\gamma_{\rm max}$	T1	T2	T3	T4	T5	T6
$\log(n_{\rm e}\times 1\,{\rm cm}^{-3})$	6.7 ± 0.2	6.3 ± 0.2	5.52 ± 0.01	5.5 ± 0.2	5.6 ± 0.1	5.8 ± 0.1	5.8 ± 0.1	5.7 ± 0.1	5.3 ± 0.1
R [$R_{\rm S}$]	1†	1†	1†	1†	1†	1†	1†	1†	1†
B [G]	38 ± 6	30†	30†	30†	30†	30†	30†	30†	30†
p	2.4 ± 0.1	2.0 ± 0.1	2†	2†	2†	2†	2†	2†	2†
$\gamma_{\rm max}$	$>10^3$	68 ± 13	48 ± 4	1.5 ± 1.4	52 ± 0.7	43 ± 5	29 ± 4	5†	5†
$\chi^2_{\rm red}$/d.o.f.	5.0/3	2.2/4	1.1/2	4.9/2	0.6/2	0.8/2	0.7/2	5.7/1	2.0/1

Notes. The quantity $n_{\rm e}$: the electron density within the source; p: the power-law index of the electron distribution; R: the projected radius, in Schwarzschild radii, of the emitting source; B: the magnetic field intensity (G); $\gamma_{\rm max}$: the maximum Lorentz factor of the accelerated electrons in units of 10^3; $\chi^2_{\rm red}$; d.o.f.: the reduced χ^2 of the best fit, the number of free parameters †: value fixed. The uncertainties reported correspond to the 1σ confidence limits determined through MCMC sampling.

accelerated from the thermal pool that is producing the submillimeter emission, and therefore we fixed $\gamma_{\rm min}=50$. We assume a source with $1\,R_{\rm S}$ radius, a magnetic field strength of $B=30\,{\rm G}$, and a cooling time of two minutes (Table 4). A fixed cooling timescale of two minutes was motivated by the light travel time for a source with radius $1\,R_{\rm S}$: the cooling-break model assumes an equilibrium of particle acceleration and particle losses due to particle escape, and thus particles at low-energy escape the flare region before they cool. In consequence, the position of the cooling break in the spectrum corresponds to the electron energy at which the escape time is equal to the cooling time (Kardashev 1962; Yuan et al. 2003). Following Dodds-Eden et al. (2009), we assume that the escape from the system can be approximated by the dynamical timescale. This assumption, together with our assumption of a magnetic field strength of $B=30\,{\rm G}$, fixes the cooling break as follows:

$$\begin{aligned}\nu_B &= 64\cdot(B/30\,[{\rm G}])^{-3}\times10^{14}/t^2_{\rm cool}\\ &= 1.6\times10^{15}\,{\rm Hz}.\end{aligned}\quad(2)$$

This model provides a decent description of the data with acceptable physical parameters, as shown in Fig. 8. The best-fit $\log(n_{\rm e})=6.3\pm0.2$ and slope of the electron distribution, $p=2.0\pm0.1$ are in line with the density expected in the hot accretion flow of Sgr A* and the electron distribution undergoing synchrotron cooling $p\geq2$ (Kardashev 1962; Ghisellini 2013). On the other hand, the model predicts a significantly softer X-ray emission than observed. Large residuals are observed at high energy, where the model decays quickly with frequency, while the data indicate a clear excess of emission associated with the flare all the way from ~2 to ~8 keV. Therefore, this model is also unsatisfactory.

8.3. Synchrotron with a cooling break and exponential high-energy cutoff

A more realistic model is an exponential decay of the electron distribution above a certain cutoff energy. This induces a shallower spectrum at high energy. A synchrotron model with a cooling break and exponential high-energy cutoff can fit the data in an acceptable way. We call this model the PLCool$\gamma_{\rm max}$. The slope of the electron distribution is $p=2.0\pm0.2$, which is consistent with the cooling break scenario (Kardashev 1962; Ghisellini 2013). The density $n_{\rm e}=10^{5.5\pm0.1}\,{\rm cm}^{-3}$ of accelerated electrons suggests that only a fraction of the electrons in the hot accretion flow are involved in the acceleration process. Finally, the best-fit $\gamma_{\rm max}=(4.8\pm4.0)\times10^4$ induces a cutoff in the X-ray band explaining the observed X-ray faintness.

9. Time-resolved evolution of Sgr A* SED during the flare

9.1. Synchrotron with a cooling break and high-energy cutoff

Figure 9 shows the Sgr A* SED temporal evolution during the flare fitted with the PLCool$\gamma_{\rm max}$ model. Table 4 reports the maximum-likelihood fit parameters and their uncertainties from the 1σ posterior contours of the Markov chain Monte Carlo (MCMC) sampling.

For T1, T5, and T6, no X-ray flux was detected. For these three time steps, therefore, the spectrum is composed of only three data points. For T2 and T3, significant X-ray flux was observed, which allows us to determine the flux of Sgr A* in two energy bins. For T4, we binned the high-energy band to one data point. Because of the limited number of free parameters in this time-resolved analysis and in the interest of reducing the number of free parameters in our model, we fixed the magnetic field strength B and the source radius R to $B=30\,{\rm G}$ and $R=1\,R_{\rm S}$. However, we left the particle density $n_{\rm e}$ free. The particle density primarily drives the normalization of the spectrum. The magnetic field strength, radius, and particle density are degenerate in the model. Therefore an error in our assumed values of the magnetic field strength and source radius would be compensated by the electron density.

We did not attempt to model the evolution of the electron distribution self-consistently. This would require assuming an emission zone expansion, an electron injection, and an electron cooling scenario. While informative, such scenarios have been explored in one-zone models of flares before (e.g., Dodds-Eden et al. 2010; Dibi et al. 2014) and we assume that the conclusions found in these studies are applicable. The analysis of the mean SED of this flare requires a maximum acceleration $\gamma_{\rm max}\sim10^4$, and we focused our modeling on the evolution of this parameter.

The minimum acceleration of the electrons is based on the submillimeter emission and fixed at $\gamma_{\rm min}=50$. Motivated by the fit to the mean SED, we fixed the slope of the electron distribution to $p=2$. Therefore, the free parameters in the model are $n_{\rm e}$ and $\gamma_{\rm max}$. Fixing the electron distribution slope precludes the possibility to explore the changes of spectral slope shown in Fig. 6. These choices and assuming that the cooling timescale is set by the escape time of particles escaping the emission region fixes the cooling break at $\nu=1.6\times10^{15}$ Hz.

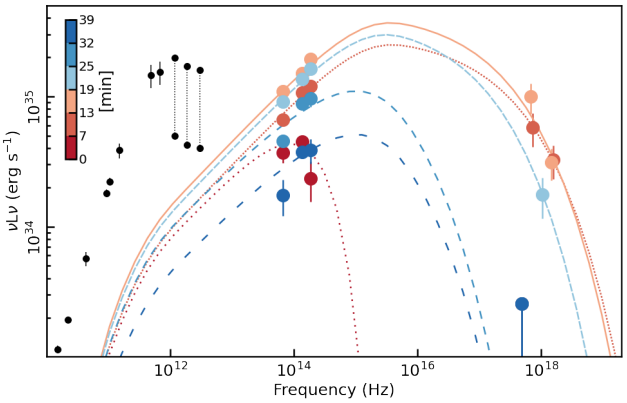

Fig. 9. Data points show the *Spitzer* + GRAVITY, and *Chandra* photometry during T1 to T6, respectively (dark red to dark blue lines). The data are corrected for the effects of absorption and dust scattering. The lines show the best-fit synchrotron with cooling break and high-energy cutoff models. During the early phases of the flare, the high-energy cutoff appears to be at low energy. During the peak of the flare, the cutoff moves to the X-ray band and then drops again to low energies toward the end of the flare. The submillimeter data shown are the same as in Fig. 4, and the color bar indicates the time and color progression.

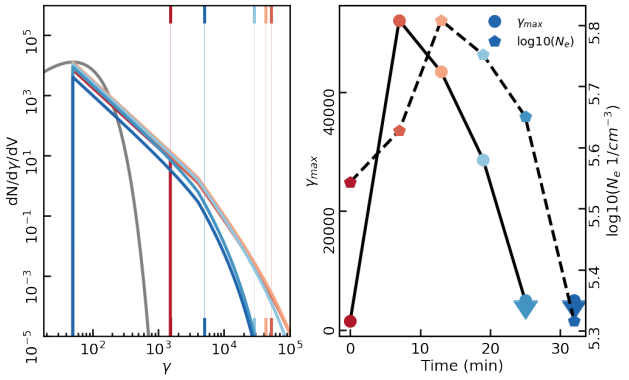

Fig. 10. *Left*: evolution of the electron distribution during the flare. The different temporal steps are plotted dark red (T1), progressing to lighter reds (T3), to light blue (T4), to dark blue (T6). The dotted lines indicate the location of $\gamma_{\rm max}$. The gray line shows a thermal distribution of electrons, peaking at $\gamma \sim 50$, which set the minimum acceleration of the electrons for the flare. *Right*: evolution of the distribution parameters $\gamma_{\rm max}$ (shown by the solid line) and $n_{\rm e}$ (shown by the dashed line).

At the start of the flare during T1 (Fig. 9), relatively bright emission was observed in the M and K bands, while fainter emission was observed in the H band and no excess emission was detected in the X-ray band. If the IR emission is produced by nonthermal synchrotron emission with a positive IR spectral slope (in νF_ν), then the lack of X-ray emission implies that the distribution of relativistic electrons must have a cutoff at high energy. The flare was bright in the M and K bands during T1, but it was barely detected in the H band, which can be understood in the framework of the PLCool$\gamma_{\rm max}$ model. If the maximum acceleration of the electrons ($\gamma_{\rm max}$) happens to be located within the K or H band, then the flux drops in the H band and no X-ray emission is expected, in line with the observational results. However, this does not explain the drop in flux between the K and H bands. The PLCool$\gamma_{\rm max}$ model only marginally matches the data, with the H-band flux being too faint compared to the K and M bands. This might be a consequence of an underestimated uncertainty for the marginal H-band detection.

In T2, the IR flux increases and the slope was consistent with a power law from the M to the H band, and significant X-ray flux was detected. The data are well-fit by the PLCool$\gamma_{\rm max}$ model, and the maximum acceleration is at frequencies slightly higher than the X-ray band. For T2 (shown by the red SED in Fig. 9), the fitted acceleration reaches its maximal value $\gamma_{\rm max} = (52 \pm 1) \times 10^3$. During the following interval (T3, shown by the light red SED in Fig. 9), the IR and X-ray emission are at their peaks. However, although little variation in the spectral slope was observed in the IR band, the simultaneous X-ray spectrum appears softer. Our model ascribes this to the maximum acceleration of the electrons having decreased to $\gamma_{\rm max} = (43 \pm 5) \times 10^3$. Subsequently, in T4, the flux starts to drop in both bands (shown by the light blue SED in Fig. 9). However, although the drop in the IR band is on the order ~20% (Fig. 9 and Table 4), again with little variation in the spectral slope, the flux in the X-ray band dropped by more than a factor of 3. Within the framework of the PLCool$\gamma_{\rm max}$ model, this can be ascribed to the acceleration mechanism continuing to lose the capability to accelerate electrons to the highest energies, therefore moving $\gamma_{\rm max}$ to $(29 \pm 4) \times 10^3$. This puts the high-energy cutoff in the electron distribution between the IR and X-ray bands, and the X-ray emission at this time would be produced mainly by electrons above the cutoff.

No X-ray emission was observed during the subsequent intervals T5 and T6 (shown by the blue and dark blue in Fig. 9). As in T1, the IR was still bright (~5−10 mJy) and flat. The PLCool$\gamma_{\rm max}$ model reproduces this by placing the high-energy cutoff somewhere between the IR and X-ray band. We thus obtain an upper limit on $\gamma_{\rm max} < 5000$.

During these last two intervals, the M-band flux dropped faster than the K- and H-band fluxes. This resulted in a blue $K-M$ slope, which would imply a decrease of p to $p \sim 1.4$, while the $H-K$ slope was consistent with $p \sim 2$. If taken at face value, the observed M-band flux was inconsistent with a fixed slope of $p = 2$ and is responsible for the worse χ^2 for T5 and T6. However, this may be attributable to a correlated error in the relative flux measurement resulting from a telescope slew (Sect. 6).

9.2. Temporal evolution of the electron distribution

Figure 10 reports the energy distribution of the accelerated electrons for each of the time bins during the flare. It also we shows the energy distribution of the electrons responsible for the submillimeter emission. To match the submillimeter SED of Sgr A*, we computed the spectrum assuming values within the range of parameters reported by Bower et al. (2019). For the submillimeter emission, we assumed an ambient magnetic field strength $B = 30$ G, as for the flare, and a size of $4\,R_{\rm S}$, which is consistent with the observed submillimeter size (Issaoun et al. 2019). We chose an ambient particle density $\log(n_{\rm e}) = 1.7 \times 10^5$ such that the distribution peaks at $\gamma_{\rm min} = 50$. The right panel of Fig. 10 shows that within 380 s, $\gamma_{\rm max}$ reaches its maximum value of $\gamma_{\rm max} \sim 5 \times 10^4$, indicating that the most energetic electrons are accelerated during T2. In the following intervals, the maximum Γ steadily decreases, and we can only constrain it to values below 4×10^3 once the X-ray flux has dropped below the detection limit. The electron density, plotted in the right panel of Fig. 10, reaches its maximum when the flux is the highest (T3), after which it steadily decreases.

Figure 11 shows the evolution of the time-resolved SED fitted with the PLCool$\gamma_{\rm max}$ model along with the respective electron distributions as inferred from the best fit.

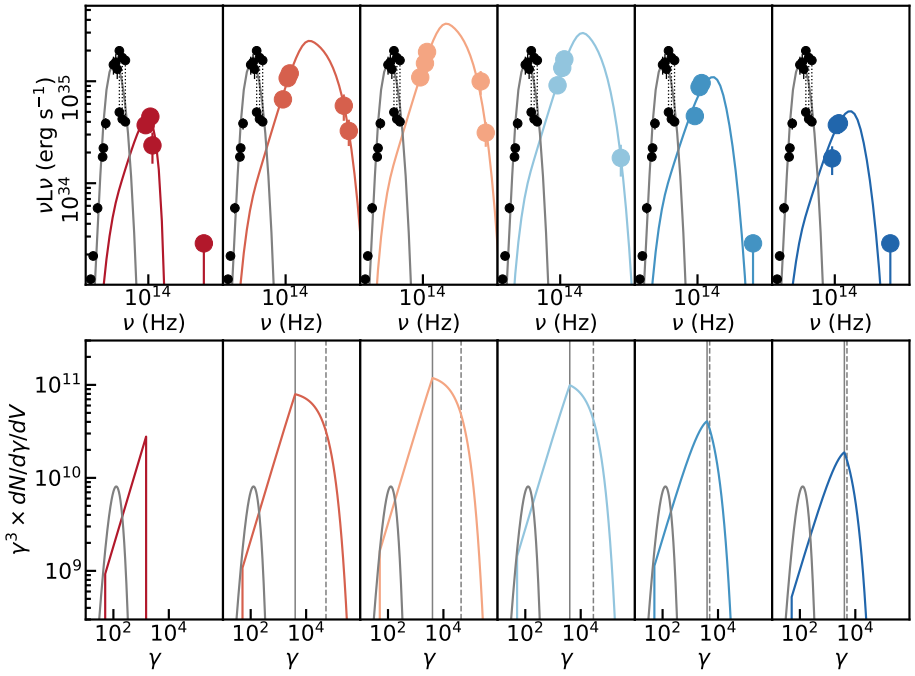

Fig. 11. Temporal evolution of the flare SED and the temporal evolution of the electron energy distribution. *Panels* (*left to right*): temporal evolution from T1 to T6. *Top row*: observed SED of the flare (colored points) and the best-fit PLCool$\gamma_{\rm max}$ model (colored lines). The black points indicate the submillimeter SED of Sgr A⋆, with the same data as in Fig. 4. The thin gray line shows a thermal synchrotron spectrum matching the submillimeter data. *Bottom row*: electron energy distribution of the respective synchrotron spectra in the top row. Colored lines show the best-fit PLCool$\gamma_{\rm max}$ models; the thin gray line shows the electron energy distribution of the thermal spectrum. The positions of the cooling break and $\gamma_{\rm max}$ are indicated with solid and dashed gray lines, respectively. To highlight the location of the breaks in the distributions, the cooling break, and the maximum acceleration the electron distribution is multiplied by a factor γ^3.

9.3. Alternative model: Synchrotron self-Compton scattering of submillimeter photons

An alternative scenario to explain the temporal evolution of Sgr A⋆ variability is proposed by Witzel et al. (2021). Using a comprehensive statistical sample of variability data at submillimeter, IR, and X-ray wavelengths, the authors discussed a strongly variable one-zone synchrotron model[6] at submillimeter to NIR wavelengths that explains the X-ray emission by IC emission. More precisely, submillimeter synchrotron photons are upscattered to the X-ray regime by the same electron population that is responsible for the synchrotron emission. This model was motivated by the following two facts: First, a compact, self-absorbed synchrotron source has the conditions necessary for the scattering efficiency to be significant. Second, the mechanism can explain the observed flux densities in the submillimeter, IR, and X-ray; the respective power spectral densities; and the cross-correlation properties between these bands.

One shortcoming of the analysis of Witzel et al. (2021) is its inability to explain the IR spectral indices $\alpha > -0.8$ as observed for several bright flares, among which is the flare discussed in this work. This is a consequence of relating the amplitude of the variable flux densities at IR and submillimeter wavelengths. In this model, the IR and submillimeter flux densities have been related to explain the strong correlation of X-ray photons (which are up-scattered from the submillimeter) with the IR. While this model was proposed as a baseline model that works for moderate flares at flux densities where the IR spectral indices are also described properly, Witzel et al. (2021) speculate that brighter flares with blue spectral indices are states in which up-scattered photons contribute to the SED even in the IR.

We implemented an SSC model based on a nonthermal, power-law-distributed electron energy distribution to fit the time-resolved data of July 18, 2019. This model was determined by the same parameters as the PLCool$\gamma_{\rm max}$ model, but it differs fundamentally from the synchrotron models above: the synchrotron part of the spectrum is located in the submillimeter (i.e., the SSC model predicts correlated submillimeter variability during this IR and X-ray flaring episode), and the IR and X-ray emission is explained through IC up-scattered photons.

In this case the parameters are also degenerate: at different electron densities $n_{\rm e}$ the source parameters B, R, and the energy range $\gamma_{\rm min}$ to $\gamma_{\rm max}$ can be chosen such that the IR to X-ray IC spectrum is reproduced as measured. However, for $n_{\rm e} < 10^9\,{\rm cm}^{-3}$ the synchrotron component significantly exceeds observed submillimeter emission levels. Therefore, we fixed the slope of the electron energy distribution to $p = 3.1$, which is consistent with the posterior of the analysis by Witzel et al. (2021). We then chose initial conditions with tight bounds such that the submillimeter luminosity remains within the range of observed submillimeter flares, and all the parameters show a continuous progression in time.

In T2–T4, where X-ray emission was detected, all other parameters besides p were left free in the fits of the SEDs. We additionally fixed $\gamma_{\rm max}$ in T1 and T5, R for T1, T4, and T6, and B for T5 and T6. To derive reliable uncertainties for T2–T4, we probed the parameter space with an MCMC sampler after lifting the bounds. The results are listed in Table 5, and the resulting SEDs and time series of parameters are shown in Figs. 12 and 13.

10. Discussion

This paper discusses the first Sgr A⋆ flare that has been continuously observed from 4.5 µm to 1.65 µm in the NIR and from 2 keV to 70 keV in the X-ray band. Compared to previously studied flares simultaneously observed in the X-ray and IR bands, this flare is exceptional for its remarkable IR brightness, relative X-ray faintness, and short duration.

10.1. Slope variability in the IR band during the flare

The IR spectrum of the flare showed an increasing spectral index with increasing flux density. During the onset of the flare, the

[6] In this scenario, this highly variable component contributes to the submillimeter, but cannot entirely explain the observed submillimeter flux density levels. A second electron population is required to explain the SED at radio to submillimeter wavelengths, and the observed submillimeter flux density is the result of the superposition of both components.

Table 5. Best-fit parameters of the fit of the SED with the SSC model.

	Time resolved					
	T1	T2	T3	T4	T5	T6
$\log(n_e \times 1\,\mathrm{cm}^{-3})$	10.0	10.0 ± 0.5	10.1 ± 0.4	10.0 ± 0.2	10.0	9.8
R µas	15†	15 ± 8	16 ± 8	16†	12	12†
B G	8.2	8 ± 6	8 ± 5	7 ± 10	8.0†	8.0†
p	3.1†	3.1†	3.1†	3.1†	3.1†	3.1†
$\gamma_{\max}$	180†	500 ± 100	470 ± 80	360 ± 70	230†	243
$\gamma_{\min}$	5.2	6.1 ± 1.8	5.4 ± 1.1	6.1 ± 0.9	7.4	7.8
χ^2_{red}; d.o.f.	6.7	0.1	2.7	0.9	0.2	0.4

Notes. The quantity n_e: the electron density within the source; p: the power-law index of the electron distribution; R: the projected radius, in µas, of the emitting source; B: the magnetic field intensity (G); $\gamma_{\max}$: the maximum Lorentz factor of the accelerated electrons; $\gamma_{\min}$: the minimum Lorentz factor of the accelerated electrons; χ^2_{red}; d.o.f.: the reduced χ^2 and number of free parameters of the best-fit †: value fixed.

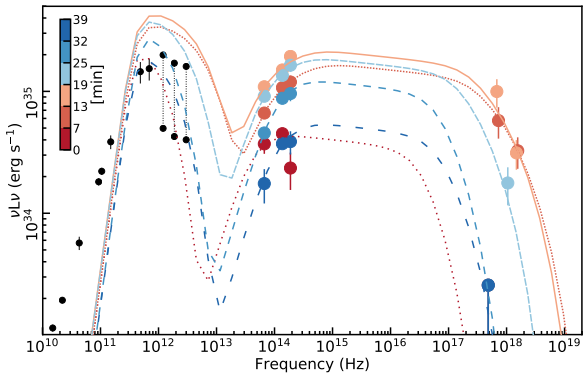

Fig. 12. SEDs of the best-fit SSC models. The colors correspond to T1 to T6 as shown in the color bar. The colored point show the observed data for each time. The dark points show the submillimeter SED of Sgr A* with the same data as in Fig. 4. As in the models involving only synchrotron emission, the flare evolution can largely be explained by progression of the electron density n_e and high-energy cutoff $\gamma_{\max}$.

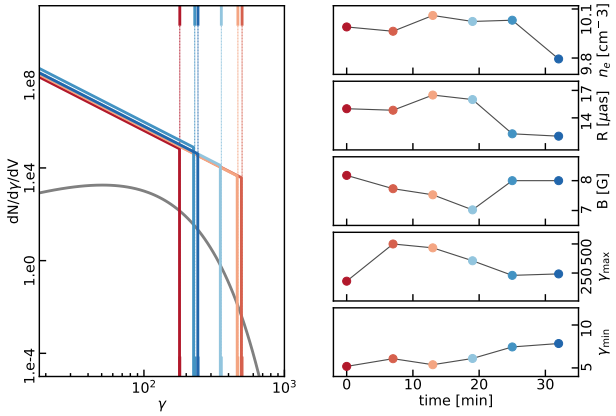

Fig. 13. SSC parameter evolution during flare, analogous to Fig. 10. *Left*: evolution of the electron distribution during the flare. The dash-dotted lines indicate the location of $\gamma_{\max}$. The gray line shows the thermal distribution of electrons, peaking at $\gamma \sim 50$, which sets the minimum acceleration of the electrons for the flare. *Right*: evolution of the model parameters n_e, R, B, $\gamma_{\max}$, and $\gamma_{\min}$. For the SSC models $\gamma_{\max}$ is significantly lower and n_e significantly higher than for the PLCool$\gamma_{\max}$ model.

ratio of the H-band flux to the M- and K-band fluxes was low. This resulted in a kink in the intra-IR spectrum. The $H-K$ slope seemed to increase with flux density, being the bluest when the flare was the brightest and decreased again toward the end of the flare. Such a flux correlation has been discussed in previous works. While Hornstein et al. (2007) measured a constant spectral slope $\nu F_\nu \propto \nu^{0.5}$ independent of flux density, Eisenhauer et al. (2005), Gillessen et al. (2006), and Genzel et al. (2010) confirmed $\nu F_\nu \propto \nu^{0.5}$ at high flux density but argued for a flux-dependent $\nu F_\nu \propto \nu^{-1\ldots-3}$ at lower flux density. The statistical analysis of the M- and K-band flux distributions presented in Witzel et al. (2018) favored a variable, flux-dependent spectral index. Our work adds further evidence for a flux-dependent spectral index. Small changes in the spectral slope that be explained either by stochastic fluctuation or a flux-dependent scaling. We also found a kink in the intra-IR spectral slope during T1. Despite the difficulty of obtaining reliable flux measurements at very low flux from AO photometry, the variation is formally significant (>1σ, Fig. 7).

10.2. Single zone emission model for Sgr A*

Using our fast numerical implementation of a one-zone emitting source, we explored a variety of models, at first regardless of their physicality in the context of the Sgr A* accretion flow. All our models require a set of parameters describing the ambient conditions as follows: (i) electron density n_e; (ii) magnetic field strength B; (iii) radius R of the emitting source, assumed to be spherical; and (iv) an energy distribution of accelerated electrons described by a set of parameters. For a thermal scenario, the distribution is characterized by a single parameter: the temperature of the electrons. For a power-law distribution, at least two parameters are required: the slope of the distribution and one or two normalization constants ($\gamma_{\min}$, $\gamma_{\max}$). The normalization constants can be interpreted in a physical sense: if the distribution is generated from a process which accelerates particles, then the minimum Lorentz factor $\gamma_{\min}$ can be interpreted as the ambient Lorentz factor of the particles. Similarly, the maximum Lorentz factor $\gamma_{\max}$ can be interpreted as a maximum length scale on which the particles are accelerated. Furthermore, the power-law distribution can have more than one slope. Such a broken power-law distribution is for instance assumed in the PLCool$\gamma_{\max}$ model, where synchrotron cooling is expected to induce a change of $p_2 = p_1 - 1$ at the cooling break.

Before reaching the observer, the synchrotron radiation can be up-scattered by a population of relativistic electrons and

produce an IC component. For example, for synchrotron one-zone models that take into account the respective SSC component, there are three different ways of obtaining simultaneous IR and X-ray emission.

1. The emission in both bands is entirely dominated by synchrotron emission. We refer to scenarios of this type as SYN–SYN scenario. In such scenarios, the photon index observed in the X-ray band should be steeper by 0.5 than the simultaneous IR value (as a consequence of the cooling break).
2. The emission in the IR is synchrotron emission, and the X-ray emission is SSC emission. We refer to these scenarios as SYN–SSC scenario.
3. The emission in both bands is entirely dominated by the IC component of the SSC emission. We refer to such a scenario as SSC–SSC scenario.

10.3. Constraints from the simultaneous IR and X-ray photon indices and flux ratios

A major problem for the SYN–SYN and the SSC models is the combination of (i) the observed positive IR slope, (ii) the observed negative X-ray slope, and (iii) the large flux ratio of IR to X-ray.

Taken at face value, the difference in X-ray to IR slopes would be perfectly consistent with a synchrotron model with a cooling break in the electron distribution (Dodds-Eden et al. 2009). However, such a model cannot at the same time reproduce the flux ratio of the IR to X-ray (Sect. 8.1).

The observed luminosity in both bands sets parameter regimes for which the three scenarios match the observed spectrum:

- To be dominated by synchrotron emission in both bands, the maximum Lorentz factor $\gamma_{\rm max}$ is required to be $\gg 10^4$.
- To be dominated by synchrotron emission in the IR and by SSC in the X-ray, $\gamma_{\rm max}$ must be rather low. The frequency at which the synchrotron emission peaks scales $\nu_{\rm c}(B) \times \gamma_{\rm max}^2$. Therefore a large magnetic field $\gg 10^3$ G is needed to shift the synchrotron peak into the IR.
- Similarly, to be dominated by SSC in both bands, $\gamma_{\rm max}$ cannot be too large. However, because the synchrotron emission does not need to be shifted into the NIR, the constraints on the magnetic field can be relaxed. Nevertheless, to sustain high SSC flux from IR to X-ray, the particle density has to be $\gg 10^9\,{\rm cm}^{-3}$.

10.3.1. The SYN–SSC scenario

The SYN–SSC scenario has severe problems: First, it requires magnetic fields of $\sim 10^4$ G, source regions around $\sim 0.001\,R_{\rm S}$, and densities $\sim 10^{12}\,{\rm cm}^{-3}$. These parameters are extreme compared to the submillimeter ambient conditions. Even ignoring this, the synchrotron cooling timescale in such a strong magnetic field is on the order of 0.1 s in the IR and on the order of 1 ms in the X-ray. Even though flares of Sgr A* are highly variable, spikes on timescales shorter than tens of seconds have never been observed in the IR band. We attribute this lack of short timescale, IR variability to the effects of the cooling time of the electrons, which smooth out any variation shorter than a few seconds. We rule out Dodds-Eden et al. (2009) and Dibi et al. (2014), that is, the scenario in which the IR flare is generated from synchrotron emission with a thermal distribution and the X-ray flare is SSC. This is a direct consequence of the negative X-ray spectral slope. If the observed X-ray slope were flat or positive, the requirement of a $\gamma_{\rm max} < 10^2$ would be relaxed. This is because for a positive or flat spectral slopes the emission can stem from the rising or flat part of SSC spectrum. In turn, this relaxes the requirement for very large magnetic fields because the peak of the synchrotron component at $\nu_{\rm max,syn}$ can be shifted by $\gamma_{\rm max}$ as well and not only by the magnetic field.

10.3.2. The SSC–SSC scenario

In the picture of the time-dependent model of Witzel et al. (2021), which can successfully describe the flux density distributions and the auto-correlation and cross-correlation properties of the light curves, the fast IR variability is the result of a quickly varying $\gamma_{\rm max}$ that truncates the synchrotron spectrum. In order to link the IR variability amplitudes at longer timescales with the submillimeter and X-ray regimes, an overall $\alpha = -1$ is required that–depending on the brightness–steepens toward the IR owing to the $\gamma_{\rm max}$ cutoff. Flatter IR spectral indices of $\alpha > -0.8$ as reported here are not possible without the up-scattered spectrum contributing to the IR.

The 2019-07-17 flare requires an even more extreme scenario in that it shows a very bright IR flare in combination with moderate X-ray luminosity. This particular configuration requires the range of the SSC component of the spectrum to be limited such that its decreasing flank falls into the 2–8 keV range. For the fit, this is achieved by restricting $\gamma_{\rm max}$ to lower values such that the IR is not a superposition of direct synchrotron and scattered photons anymore but is dominated by the SSC component entirely. To then reach the high IR flux density of this flare while keeping B and R at levels that do not lead to unobserved, high submillimeter luminosities, $n_{\rm e} > 10^{10}\,{\rm cm}^{-3}$ is required. While much higher than the typical, average electron densities derived from modeling the radio to submillimeter SED of Sgr A* with synchrotron emission from a thermal electron distribution (ambient $n_{\rm e} < 10^7\,{\rm cm}^{-3}$; Bower et al. 2019), $n_{\rm e} > 10^{10}\,{\rm cm}^{-3}$ is not out of the question: Mościbrodzka & Falcke (2013) discussed mid-plane densities of $n_{\rm e} = 10^9\,{\rm cm}^{-3}$, and Yoon et al. (2020) used $10^{-13}\,{\rm gcm}^{-3}$, which corresponds to $5.9 \times 10^{10}\,{\rm cm}^{-3}$.

10.3.3. The SYN–SYN scenario

The SYN–SYN scenario realized via the PLCool$\gamma_{\rm max}$ model requires $\gamma_{\rm max} \sim 50\,000$ and an exponential decay rather than a sharp cutoff (see Fig. 11). Because our data constrains the fit in the optically thin part of the spectrum, we can infer only the total number of electrons rather than the radius and electron density independently. Fixing the source radius to $1\,R_{\rm S}$, we obtained an estimate of the electron density. By assuming a cooling timescale of two minutes and by requiring a cooling break between the IR and the X-ray, the magnetic field is constrained to $B \sim 1$ to 100 G[7]. Under these assumptions, the plasma parameters required are comparable to the submillimeter ambient parameters inferred from the submillimeter SED (e.g., Yuan et al. 2003; Bower et al. 2019). This model requires that the process accelerating the electrons generates Lorentz factors increased from ambient conditions by a factor $>10^3$ and does so without alteration of the ambient plasma parameters on large scales. The best-fit model for the mean SED sets a direct constraint on $\gamma_{\rm max}$. As discussed in Sect. 8.2, this is a consequence of the high flux in the IR together with moderate flux in X-ray.

[7] This is sensitive to our choice of the cooling timescale because the break frequency scales as $\nu_{\rm break} \propto 1/t_{\rm cool}^2$.

Under the model assumptions, our observations place limits on the maximum acceleration of the flare-generating process (as done by Ponti et al. 2017). Notably, this flare mechanism does not produce any relevant submillimeter flux. Therefore, it does not predict any direct effect on the submillimeter light curve and observable accretion flow[8]. For our choice of $R = 1\,R_S$, the SSC component of the flare peaks at around 10^{23} Hz (corresponding to GeV energy band), with a peak luminosity of $\sim 10^{34}$ erg s^{-1} (Fig. A.1). Unfortunately, this implies that the expected SSC luminosity is too faint to be observable by, for instance, the *Fermi* satellite (Malyshev et al. 2015).

10.4. Temporal evolution of the flare

10.4.1. Temporal evolution in the SSC–SSC scenario

The Compton component of the SSC–SSC model is sensitive to where the synchrotron emission becomes optically thick. Therefore, such a model places strong constraints on the synchrotron part of the spectrum, which is expected to reproduce the emission in the submillimeter band. Unfortunately, our campaign has no coverage of the submillimeter band. Therefore, we cannot uniquely derive the best-fit solution, but instead can only constrain the parameters by assuming typical values for the submillimeter emission. Keeping the magnetic field, the electron density and the radius thus constrained, we modeled the light curve of the flare by selecting a suitable local minimum. The temporal evolution of flux densities is then mostly driven by the variation of $\gamma_{\rm max}$, which determines the width of the synchrotron spectrum and, as a consequence, scales the X-ray flux.

The SSC–SSC scenario predicts that a high submillimeter flux density excursion is associated with the flare of 2019-07-17, that is, that the submillimeter exhibits temporal correlation with the IR light curve. Depending on the exact combination of parameters, the submillimeter light curve may lag slightly behind the IR and X-ray, comparable to the effects of source expansion discussed by Witzel et al. (2021).

The "kink" in the X-ray spectrum of the first data point cannot be explained by SSC–SSC scenario because it either requires a SSC component that is too narrow, or an extension of the synchrotron component into the IR for only the first data point. Except for this cutoff between the K and H band of T1, the model can closely fit the measurements. In particular, it reproduces the frequency-dependent spectral index in the IR that changes from the very blue index between the M and K band to a flatter $K-H$ index.

Bower et al. (2018) showed in a study of ALMA polarization data that the observed Faraday rotation is consistent with the rotation measure expected from a radiatively inefficient accretion flow (RIAF) with $\dot{M} = 10^{-8}\,M_\odot\,{\rm y}^{-1}$, or $\dot{M} = 3 \times 10^{-16}\,M_\odot\,{\rm s}^{-1}$. Assuming a proton to electron ratio of unity, the changes in electron density as suggested by the temporal evolution described in this work of $\Delta n_{\rm e} \approx 6.3 \times 10^9\,{\rm cm}^{-3}$ over a region of $\sim 1.5\,R_S$ require an additional mass $\Delta M \approx 1.3 \times 10^{-10}\,M_\odot$. The average accretion flow would require >100 h to provide this much mass, but in this scenario the density evolves within less than 30 min. This suggests that interpreting the flare in the context of the SSC–SSC model makes the implicit assumption of moments of extraordinary accretion far exceeding the average accretion flow.

10.4.2. Temporal evolution of the SYN–SYN scenario

The time-resolved spectra were fitted assuming a constant magnetic field strength and source size because of the degeneracy with the electron density. Therefore, in our modeling, the normalization of the spectrum is mainly determined by the electron density. Similar to the model discussed by Dodds-Eden et al. (2010) and Ponti et al. (2017), this scenario assumes an episode of particle injection with large $\gamma_{\rm max}$, which sustains the X-ray emission against the very short cooling timescales. The quality of the data and the degeneracy of the model parameters do not allow us to explicitly model the evolution of the radius and magnetic field intensity in addition to the electron density (e.g., Dodds-Eden et al. 2010; Ponti et al. 2017). Therefore, it remains to be verified whether the findings of Dodds-Eden et al. (2010) and Ponti et al. (2017) hold and are applicable here as well.

Although it appears sharper than the model predicts, the apparent kink in the IR spectrum at T1 is attributed to the truncated electron distribution function at $\gamma_{\rm max} \sim 500$. These observations place strong constraints on the timescales under which electron acceleration has to be maintained and on how fast it needs to vary (see Fig. 10; Ponti et al. 2017).

10.5. Concluding remarks

For both the SYN–SYN and SSC–SSC models, this flare sets strong requirements on the mechanism responsible for its emission. Either the flare requires acceleration of electrons by a factor of $>10^3$, or it requires electron densities increased by a factor of $10^{2...3}$ ecm^{-3} and electron density changes with respect to the submillimeter ambient conditions that cannot be explained from the average accretion flow. Furthermore, it is remarkable that in both cases, the maximum Lorentz factor plays a very important role for the temporal evolution of the flare. For the SSC–SSC scenario, $\gamma_{\rm max}$ regulates the width of the synchrotron spectrum, which in turn sets the width of the Compton component. Similarly, for the SYN–SYN scenario, the kink of the IR spectrum for T1, the high IR-to-X-ray flux ratio, and the X-ray slope are dictated by the evolution of $\gamma_{\rm max}$. A similar evolution of the SED was observed during another flare detected simultaneously in the IR and X-ray band (Ponti et al. 2017). Both models make strong predictions about the presence of a direct submillimeter counterpart. The SSC–SSC scenario would be ruled out in the absence of a strong flux increase by a factor of 2 to 3, while the extrapolation to the submillimeter band of the SYN–SYN model predicts no significant contribution to the submillimeter emission; a possible variation of the magnetic field however might induce some degree of correlated variations in the submillimeter band (Dodds-Eden et al. 2010; Ponti et al. 2017). All of our modeling has ignored the expected modulation of the light curve from the relativistic motion of the flare itself and other relativistic effects expected in the proximity of the BH (GRAVITY Collaboration 2018, 2020a). For the SYN–SYN scenario, the modulation of the light curve by relativistic boosting does merely translate into a variation of the assumed parameters. The same is not true for the SSC–SSC scenario: the Compton scattering occurs in the flare rest frame, while the synchrotron emission is observed from

[8] This is strictly true only if the assumptions made here are valid. Ponti et al. (2017) discussed a brighter X-ray flare, where the magnetic field strength was consistent with the ambient value before and after the flare, while it significantly drops at the peak of the flare. If the magnetic field strength dropped at the peak of the flare (possibly as a consequence of magnetic reconnection) in a significant fraction of the volume producing the emission in the submillimeter band, then a drop in the submillimeter emission might be expected to be observed at the peak of the flare as a consequence of the smaller magnetic field strength (Dodds-Eden et al. 2010).

outside. Consequently, the SSC component of a relativistic hot spot may be lowered while the synchrotron component may be increased (or vice versa). Future modeling of such a scenario should take this effect into account.

In light of the new data, we rule out the SYN–SSC scenario for this flare because it requires nonphysical model parameters and would imply NIR variability on timescales not observed. We consider that neither the SYN–SYN nor the SSC–SSC models can be strictly ruled out. However, the SSC–SSC scenarios requires very high local over-densities in the accretion flow and a density variation that cannot be explained with the average mass accretion. It therefore requires an extraordinary accretion event together with moderate particle acceleration.

The SYN–SYN model does not require extraordinary accretion, but requires particle acceleration from Lorentz factors of the ambient electrons of $\gamma \sim 10$ to $\gamma \sim 10^4$. Typically discussed candidate mechanisms are either electron acceleration through magnetic reconnection, turbulent heating in shocks induced by a misalignment of BH spin and accretion flow or in shocks along an outflow/jet (Dodds-Eden et al. 2009; Dexter & Fragile 2012). Large-scale simulations of the accretion flow do not have the resolution to trace individual reconnection events, but several strategies have been developed to try to account for this (Dexter et al. 2020; Chatterjee et al. 2021). Particles in cell simulations of plasmas show that turbulence heating and magnetic reconnection can create significantly nonthermal, power-law electron distributions (Sironi & Beloborodov 2020; Wong et al. 2020; Werner & Uzdensky 2021). Interestingly, the arge-scale simulation presented by Ripperda et al. (2020) shows flare regions of a size of around 1 to $2\,R_S$ formed through magnetic reconnection with comparable field strengths to those in the toy models discussed in this work. In the SYN–SYN model, this flare places tight constraints on the maximum allowed acceleration. If no rigorous theoretical motivation for such a specific value of the maximum acceleration value is found[9], it may ultimately be viewed as too constraining to uphold the simple SYN–SYN model and it may need to be discarded in favor of more complicated models. Conversely, if the maximum acceleration of an acceleration process is rooted in a sound theoretical framework, future observations of IR bright and X-ray faint flares may provide a powerful tool to constrain the underlying acceleration physics.

Currently, there are no models that can correctly match the observed spectrum, variability, and orbital motions of the emission at the Galactic Center. Our two models shown above reproduce the SED during flares, but do not include enough physics to account for variability or orbital motions. More physically motivated GRMHD simulations show more complexity but are also not able to fully explain observations. However, in GRMHD models the NIR synchrotron photons and IC scattering are associated with spatially separate populations of electrons, an effect that is not captured in our simple one-zone models. More work is needed to combine these approaches or develop new methods to understand the emission mechanism and dynamical properties of the accretion flow at the smallest scales.

Acknowledgements. SvF thanks Giulia Focchi for her contribution to the *H*-band acquisition camera pipeline. SvF, and FW acknowledge support by the Max Planck International Research School. GP is supported by the H2020 ERC Consolidator Grant Hot Milk under grant agreement Nr. 865637. A.A. and P.G. were supported by Fundação para a Ciência e a Tecnologia, with grants reference UIDB/00099/2020 and SFRH/BSAB/142940/2018. This work is based in part on observations made with the *Spitzer* Space Telescope, which was operated by the Jet Propulsion Laboratory, California Institute of Technology under a contract with NASA. Support for this work was provided by NASA. The scientific results reported in this article are based in part on observations made by the *Chandra* X-ray Observatory. This work is based in part on observations made with *NuSTAR*, which is operated by NASA/JPL-Caltech. GGF, JLH, HAS, and SPW acknowledge support for this work from the NASA ADAP program under NASA grant 80NSSC18K0416.

[9] For instance, assuming the particles are accelerated for $1\,R_S$ with a fraction of the speed of light would yield a Lorentz factor of $\gamma(\nu) = eBR_S/m_e c^2 \times \nu/c \sim 1\times10^{10}\times\nu/c$, implying that the acceleration happens on much smaller scales.

References

Baganoff, F. K., Bautz, M. W., Brandt, W. N., et al. 2001, Nature, 413, 45
Baganoff, F. K., Maeda, Y., Morris, M., et al. 2003, ApJ, 591, 891
Barrière, N. M., Tomsick, J. A., Baganoff, F. K., et al. 2014, ApJ, 786, 46
Bouffard, É., Haggard, D., Nowak, M. A., et al. 2019, ApJ, 884, 148
Bower, G. C., Markoff, S., Dexter, J., et al. 2015, ApJ, 802, 69
Bower, G. C., Broderick, A., Dexter, J., et al. 2018, ApJ, 868, 101
Bower, G. C., Dexter, J., Asada, K., et al. 2019, ApJ, 881, L2
Boyce, H., Haggard, D., Witzel, G., et al. 2019, ApJ, 871, 161
Brinkerink, C. D., Falcke, H., Law, C. J., et al. 2015, A&A, 576, 41
Chatterjee, K., Markoff, S., Neilsen, J., et al. 2021, MNRAS, 507, 5281
Dexter, J., & Fragile, P. C. 2012, MNRAS, 432, 2252
Dexter, J., Jiménez-Rosales, A., Ressler, S. M., et al. 2020, MNRAS, 494, 4168
Dibi, S., Markoff, S., Belmont, R., et al. 2014, MNRAS, 441, 1005
Do, T., Ghez, A. M., Morris, M. R., et al. 2009, ApJ, 703, 1323
Do, T., Hees, A., Ghez, A., et al. 2019, Science, 365, 664
Dodds-Eden, K., Porquet, D., Trap, G., et al. 2009, ApJ, 698, 676
Dodds-Eden, K., Sharma, P., Quataert, E., et al. 2010, ApJ, 725, 450
Dodds-Eden, K., Gillessen, S., Fritz, T. K., et al. 2011, ApJ, 728, 37
Eckart, A., Baganoff, F. K., Morris, M., et al. 2004, A&A, 427, 1
Eckart, A., Schödel, R., Meyer, L., et al. 2006, A&A, 455, 1
Eckart, A., Schödel, R., García-Marín, M., et al. 2008, A&A, 492, 337
Eckart, A., Baganoff, F. K., Morris, M. R., et al. 2009, A&A, 500, 935
Eckart, A., García-Marín, M., Vogel, S. N., et al. 2012, A&A, 537, A52
Eisenhauer, F., Genzel, R., Alexander, T., et al. 2005, ApJ, 628, 246
Falcke, H., Goss, W. M., Matsuo, H., et al. 1998, ApJ, 499, 731
Fazio, G. G., Hora, J. L., Allen, L. E., et al. 2004, ApJS, 154, 10
Fazio, G., Ashby, M., Baganoff, F., et al. 2018, The Vital Infrared to X-ray Link in the Sgr A* Accretion Flow, Spitzer Proposal
Fritz, T. K., Gillessen, S., Dodds-Eden, K., et al. 2011, ApJ, 737, 73
Fruscione, A., McDowell, J. C., Allen, G. E., et al. 2006, in Society of Photo-Optical Instrumentation Engineers (SPIE) Conference Series, eds. D. R. Silva, & R. E. Doxsey, 6270, 62701V
Garmire, G. P., Bautz, M. W., Ford, P. G., Nousek, J. A., & Ricker, G. R., Jr. 2006, in X-ray and Gamma-ray Telescopes and Instruments for Astronomy, eds. J. E. Truemper, & H. D. Tananbaum, SPIE Conf. Ser., 4851, 28
Gehrels, N. 1986, ApJ, 303, 336
Genzel, R., Schödel, R., Ott, T., et al. 2003, Nature, 425, 934
Genzel, R., Eisenhauer, F., & Gillessen, S. 2010, Rev. Mod. Phys., 82, 3121
Ghez, A. M., Wright, S. A., Matthews, K., et al. 2004, ApJ, 601, L159
Ghisellini, G. 2013, Radiative Processes in High Energy Astrophysics (Switzerland: Springer International Publishing), 873
Gillessen, S., Eisenhauer, F., Quataert, E., et al. 2006, ApJ, 640, 163
Gillessen, S., Plewa, P. M., Eisenhauer, F., et al. 2017, ApJ, 837, 30
GRAVITY Collaboration (Abuter, R., et al.) 2018, A&A, 618, L10
GRAVITY Collaboration (Abuter, R., et al.) 2019, A&A, 625, L10
GRAVITY Collaboration (Bauböck, M., et al.) 2020a, A&A, 635, A143
GRAVITY Collaboration (Jiménez-Rosales, A., et al.) 2020b, A&A, 643, A56
GRAVITY Collaboration (Abuter, R., et al.) 2020c, A&A, 638, A120
GRAVITY Collaboration (Abuter, R., et al.) 2021, A&A, 647, A59
Harrison, F. A., Craig, W. W., Christensen, F. E., et al. 2013, ApJ, 770, 103
Hora, J. L., Witzel, G., Ashby, M. L., et al. 2014, ApJ, 793, 120
Hornstein, S. D., Matthews, K., Ghez, A. M., et al. 2007, ApJ, 667, 900
Ingalls, J. G., Krick, J. E., Carey, S. J., et al. 2012, in Space Telescopes and Instrumentation 2012: Optical, Infrared, and Millimeter Wave, eds. M. C. Clampin, G. G. Fazio, H. A. MacEwen, J. Oschmann, & M. Jacobus, SPIE Conf. Ser., 8442, 84421Y
Issaoun, S., Johnson, M. D., Blackburn, L., et al. 2019, ApJ, 871, 30
Jin, C., Ponti, G., Haberl, F., & Smith, R. 2017, MNRAS, 468, 2532
Jin, C., Ponti, G., Haberl, F., Smith, R., & Valencic, L. 2018, MNRAS, 477, 3480
Kardashev, N. S. 1962, Sov. Astron., 6, 317
Kormendy, J., & Ho, L. C. 2013, ARA&A, 51, 511
Li, Y.-P., Yuan, F., & Wang, Q. D. 2017, MNRAS, 468, 2552
Liu, H. B., Wright, M. C. H., Zhao, J.-H., et al. 2016, A&A, 593, A107
Loeb, A., & Waxman, E. 2007, JCAP, 2007, 011

Malyshev, D., Chernyakova, M., Neronov, A., & Walter, R. 2015, A&A, 582, A11
Markoff, S., Falcke, H., Yuan, F., & Biermann, P. L. 2001, A&A, 379, L13
Marrone, D. P., Baganoff, F. K., Morris, M. R., et al. 2008, ApJ, 682, 373
Meyer, L., Do, T., Ghez, A., et al. 2009, ApJ, 694, 87
Mościbrodzka, M., & Falcke, H. 2013, A&A, 559, L3
Mossoux, E., Grosso, N., Bushouse, H., et al. 2016, A&A, 589, A116
Neilsen, J., Nowak, M. A., Gammie, C., et al. 2013, ApJ, 774, 42
Nowak, M. A., Neilsen, J., Markoff, S. B., et al. 2012, ApJ, 759, 95
Pacholczyk, A. G. 1970, Radio Astrophysics. Nonthermal Processes in Galactic and Extragalactic Sources (San Francisco: Freeman)
Pandya, A., Zhang, Z., Chandra, M., & Gammie, C. F. 2016, ApJ, 822, 34
Ponti, G., De Marco, B., Morris, M. R., et al. 2015, MNRAS, 454, 1525
Ponti, G., George, E., Scaringi, S., et al. 2017, MNRAS, 468, 2447
Porquet, D., Predehl, P., Aschenbach, B., et al. 2003, A&A, 407, L17
Porquet, D., Grosso, N., Predehl, P., et al. 2008, A&A, 488, 549
Quataert, E. 2002, ApJ, 575, 855
Ripperda, B., Bacchini, F., & Philippov, A. A. 2020, ApJ, 900, 100
Sironi, L., & Beloborodov, A. M. 2020, ApJ, 899, 52
Stone, J. M., Marrone, D. P., Dowell, C. D., et al. 2016, ApJ, 825, 32
Trap, G., Goldwurm, A., Dodds-Eden, K., et al. 2011, A&A, 528, A140
Verner, D. A., Ferland, G. J., Korista, K. T., & Yakovlev, D. G. 1996, ApJ, 465, 487
von Fellenberg, S. D., Gillessen, S., Graciá-Carpio, J., et al. 2018, ApJ, 862, 129
Weisskopf, M. C., Tananbaum, H. D., Van Speybroeck, L. P., & O'Dell, S. L. 2000, in X-ray Optics, Instruments, and Missions III, eds. J. E. Truemper, & B. Aschenbach, SPIE Conf. Ser., 4012, 2
Werner, G. R., & Uzdensky, D. A. 2021, ArXiv e-prints [arXiv:2106.02790]
Werner, M. W., Roellig, T. L., Low, F. J., et al. 2004, ApJS, 154, 1
Wilms, J., Allen, A., & McCray, R. 2000, ApJ, 542, 914
Witzel, G., Martinez, G., Hora, J., et al. 2018, ApJ, 863, 15
Witzel, G., Martinez, G., Willner, S. P., et al. 2021, ApJ, 917, 73
Wong, K., Zhdankin, V., Uzdensky, D. A., Werner, G. R., & Begelman, M. C. 2020, ApJ, 893, L7
Xu, Y.-D., Narayan, R., Quataert, E., Yuan, F., & Baganoff, F. K. 2006, ApJ, 640, 319
Yoon, D., Chatterjee, K., Markoff, S. B., et al. 2020, MNRAS, 499, 3178
Yuan, F., Quataert, E., & Narayan, R. 2003, ApJ, 598, 301
Yusef-Zadeh, F., Roberts, D., Wardle, M., Heinke, C. O., & Bower, G. C. 2006, ApJ, 650, 189
Yusef-Zadeh, F., Wardle, M., Heinke, C., et al. 2008, ApJ, 682, 361
Yusef-Zadeh, F., Bushouse, H., Wardle, M., et al. 2009, ApJ, 706, 348

[1] Max Planck Institute for Extraterrestrial Physics, Giessenbachstrasse 1, 85748 Garching, Germany
[2] LESIA, Observatoire de Paris, Université PSL, CNRS, Sorbonne Université, Université de Paris, 5 Place Jules Janssen, 92195 Meudon, France
[3] Max Planck Institute for Astronomy, Königstuhl 17, 69117 Heidelberg, Germany
[4] 1st Institute of Physics, University of Cologne, Zülpicher Strasse 77, 50937 Cologne, Germany
[5] Univ. Grenoble Alpes, CNRS, IPAG, 38000 Grenoble, France
[6] Universidade de Lisboa – Faculdade de Ciências, Campo Grande, 1749-016 Lisboa, Portugal
[7] Faculdade de Engenharia, Universidade do Porto, Rua Dr. Roberto Frias, 4200-465 Porto, Portugal
[8] European Southern Observatory, Karl-Schwarzschild-Strasse 2, 85748 Garching, Germany
[9] European Southern Observatory, Casilla 19001, Santiago 19, Chile
[10] Sterrewacht Leiden, Leiden University, Postbus 9513, 2300 RA Leiden, The Netherlands
[11] Departments of Physics and Astronomy, Le Conte Hall, University of California, Berkeley, CA 94720, USA
[12] CENTRA – Centro de Astrofísica e Gravitação, IST, Universidade de Lisboa, 1049-001 Lisboa, Portugal
[13] INAF-Osservatorio Astronomico di Brera, Via E. Bianchi 46, 23807 Merate, LC, Italy
[14] Department of Astrophysical & Planetary Sciences, JILA, University of Colorado, Duane Physics Bldg., 2000 Colorado Ave, Boulder, CO 80309, USA
[15] Department of Particle Physics & Astrophysics, Weizmann Institute of Science, Rehovot 76100, Israel
[16] Institute of Astronomy, Madingley Road, Cambridge CB3 0HA, UK
[17] Department of Physics, Technical University Munich, James-Franck-Strasse 1, 85748 Garching, Germany
[18] Max Planck Institute for Radio Astronomy, Auf dem Hügel 69, 53121 Bonn, Germany
[19] Center for Astrophysics | Harvard & Smithsonian, 60 Garden St., Cambridge, MA 02138, USA
[20] MIT Kavli Institute for Astrophysics and Space Research, Cambridge, MA 02139, USA
[21] Department of Physics, McGill University, 3600 University St., Montreal, QC H3A 2T8, Canada
[22] McGill Space Institute, 3550 University St., Montreal, QC H3A 2A7, Canada
[23] Spitzer Science Center, California Institute of Technology, Pasadena, CA 91125, USA
[24] UCLA Galactic Center Group, Physics and Astronomy Department, University of California, Los Angeles, CA 90024, USA
[25] Department of Astronomy, University of Illinois, 1002 West Green Street, Urbana, IL 61801, USA
[26] Anton Pannekoek Institute for Astronomy, University of Amsterdam, 1098 XH Amsterdam, The Netherlands
[27] Columbia Astrophysics Laboratory, Columbia University, 550 West 120th Street, Room 1027, New York, NY 10027, USA
[28] Bard College Physics Program, 30 Campus Road, Annandale-On-Hudson, NY 12504, USA
[29] Villanova University, Department of Physics, Villanova, PA 19085, USA
[30] Cahill Center for Astronomy and Astrophysics, California Institute of Technology, Pasadena, CA 91125, USA
[31] Jet Propulsion Laboratory, California Institute of Technology, 4800 Oak Grove Drive, MS 169-224, Pasadena, CA 91109, USA

Appendix A: Synchrotron self-Compton of the SYN–SYN scenario

The SSC component of the SYN–SYN scenario peaks at frequencies higher than the X-ray band. Unfortunately, for the parameter ranges we assume (Table 4), this peak is not bright enough to be detectable in the GeV bands by for example *Fermi* (e.g., Malyshev et al. 2015). However, it poses a possibility to constrain the radius and the particle density of the otherwise optically thin spectrum. At small enough radii and high enough densities, the falling flank of the SSC spectrum starts to contribute to the 2−70 keV band of *NuSTAR*. For instance, at B = 30G, the emission region is constrained to ∼0.3 R_S. This demonstrates the importance of further parallel NIR–X-ray observations with as wide as possible spectral range.

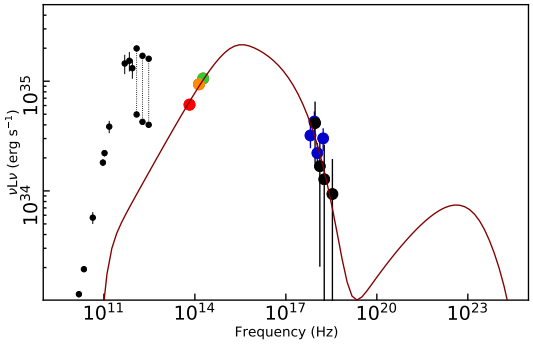

Fig. A.1. Mean SED of Sgr A* during the flare, including the SSC component of the PLCoolγ_{max} model. This component peaks at $\nu \sim 10^{23}$ Hz.

Appendix B: Accounting for the acquisition camera transmission curve and the different spectral slopes of S2 and Sgr A*

The GRAVITY flux measurements derived in both bands are measurements of the flux ratios of the S2 and Sgr A*. The spectral dependence of the reddened flux of Sgr A* and S2 can be approximated as a power law with different indices:

$$F_{S2}(\lambda) = F_{S2_0} \cdot \frac{\lambda}{\lambda_0}^{\alpha_{S2}}$$
$$F_{Sg}(\lambda) = F_{Sg_0} \cdot \frac{\lambda}{\lambda_0}^{\alpha_{Sg}}, \quad \text{(B.1)}$$

where F_{x_0} denotes the flux of the respective source at wavelength λ_0. For S2, the spectral slope α_{S2} can be determined from the NACO photometry in the H and K bands (e.g., Gillessen et al. 2017).

To account for the effect of different spectral slopes on the flux ratio in the H band, we have to take the filter curves of the acquisition camera, the VLTI, and GRAVITY into account. This can be achieved by expressing the flux of both sources on the acquisition camera detector as functions of the respective effective wavelengths as follows:

$$F_{S2}(\lambda) = F_{K,S2} \cdot \frac{\lambda_{eff,S2}}{\lambda}^{\alpha_{S2}}$$
$$F_{SgrA}(\lambda) = F_{K,SgrA} \cdot \frac{\lambda_{eff,S2}}{\lambda}^{\alpha_{SgrA}}. \quad \text{(B.2)}$$

Here the effective wavelength, assuming a power-law flux dependence, is given by

$$\lambda_{eff}(\alpha) = \frac{\int F_\lambda(\alpha) \cdot \lambda \, d\lambda}{\int F_\lambda(\alpha) d\lambda}, \quad \text{(B.3)}$$

where $F_\lambda = F_{source}(\alpha) \cdot T(\lambda)$ is the power-law source flux multiplied by the instrument transmission $T(\lambda)$. The observed flux ratio in the H band can then be expressed as

$$r_H = \frac{\int F_{K,S2} \cdot \left(\frac{\lambda_{eff,S2}}{\lambda_K}\right)^{\alpha_{S2}} d\lambda}{\int F_{K,SgrA} \cdot \left(\frac{\lambda_{eff,SgrA}}{\lambda_K}\right)^{\alpha_{SgrA}} d\lambda}, \quad \text{(B.4)}$$

where $F_{K/H,S2}$ is the observed flux in the K band, and $\lambda_{eff,S2/SgrA}$ are the acquisition camera effective wavelength of S2 and Sgr A*. We obtain $\lambda_{eff,S2}$ in the H band using the acquisition camera transmission curve and the reddened power-law flux relation determined from NACO photometry.

Using the functional relation for the effective Sgr A* wavelength in the H band, we can rewrite this as

$$\left(\frac{\lambda_{eff,SgrA}(\alpha_{SgrA})}{\lambda_K}\right) = \left(\frac{\lambda_{eff,S2}(\alpha)}{\lambda_K}\right)^{\alpha_{S2}} \cdot \frac{r_K}{r_H}, \quad \text{(B.5)}$$

where r_K and r_H are the observed flux ratios in the H and K bands. We can numerically solve this equation for the effective wavelength $\lambda_{eff,SgrA}$. Once $\lambda_{eff,SgrA}$ and α_{SgrA} are determined, we can plug these into equation B.2 to obtain the reddened H-band flux density F_λ. We converted F_λ to flux density F_ν and deredden through the standard approach $F_{dered.} = F_{red.} \cdot 10^{0.4 \cdot m_H}$, with m_H as discussed in section 2.6.

Appendix C: Effect of the column density on the IR and X-ray spectral slope, and inferred parameters

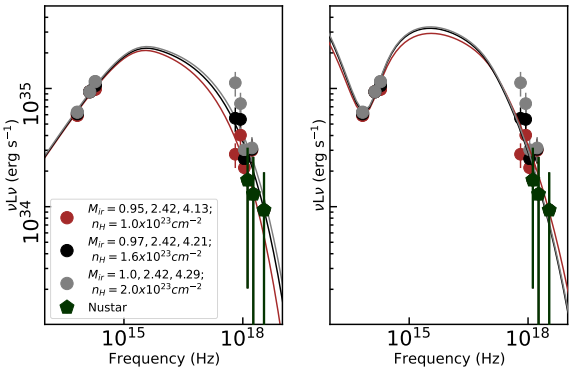

Fig. C.1. Effect of different neutral material column density: NIR data same as Figure 4. Both panels: the red, black and gray lines show the data corrected with different plausible neutral material column densities, which are reported in the legend of the left panel. The *NuSTAR* data have not been re-reduced (green pentagons) because the high-energy data is only marginally affected. The lowest energy bin from the *NuSTAR* spectrum has been removed because it might be affected by the extinction. The models in the left panel are PLCoolγ_{max} type models, the SCC-SSC type models are plotted on the right, and the color indicates the respective data set fitted.

Table C.1. Effect of different choices of the neutral absorption column density. The fit parameters for the SYN–SYN model and the SSC–SSC model derived from a least-squares fitting. The models are described in Appendix C. The reported uncertainties were derived from the covariance matrix.

Parameter	SYN–SYN model $\log_{10}(n_e)$ γ_{max}	SSC–SSC model $\log_{10}(n_e)$, B, γ_{max}
$M_{IR} = 0.95, 2.42, 4.13$; $n_H = 1.0 \times 10^{23}\,\mathrm{cm}^{-2}$	6.243 ± 0.015, 39620 ± 3808	9.75 ± 0.03, (17.1 ± 0.25) G, 276 ± 29
$M_{IR} = 0.97, 2.42, 4.21$; $n_H = 1.6 \times 10^{23}\,\mathrm{cm}^{-2}$	6.240 ± 0.011, 47179 ± 3824	9.74 ± 0.02, (19.2 ± 0.3) G, 244 ± 13
$M_{IR} = 1.0, 2.42, 4.29$; $n_H = 2.0 \times 10^{23}\,\mathrm{cm}^{-2}$	6.249 ± 0.014, 51113 ± 5436	9.74 ± 0.01, (19.5 ± 0.1) G, 245 ± 14

As discussed in Section 2.2, we chose three different column density values $n_{\mathrm{H}} = 1.0 \times 10^{23}\,\mathrm{cm}^{-2}$, $n_{\mathrm{H}} = 1.6 \times 10^{23}\,\mathrm{cm}^{-2}$, $n_{\mathrm{H}} = 2.0 \times 10^{23}\,\mathrm{cm}^{-2}$. We fitted the *Chandra* mean spectrum of the flare assuming each of the above-mentioned values of the column density and computed the respective corrections in order to de-absorb the spectrum. Similarly, we varied the infrared extinction and scaled the flux density according to the uncertainties reported in Table 2. Figure C.1, shows the de-absorbed data and the resulting fits to the data sets. For the SYN–SYN model, we assumed the same parameters as for the PLCoolγ_{max} model (see Table 4). For the SSC–SSC model, we assumed fixed radius $1R_S$, a fixed slope of the electron distribution $p = 3.1$, and a fixed minimum acceleration $\gamma_{min} = 10$. We fit the particle density, magnetic field, and maximum acceleration. Table C.1 reports the best-fit results. While the inferred parameters of the best-fit solution change slightly, the main conclusions of the paper are not affected by the choice of the specific extinction value: the SYN–SYN model requires a $\gamma_{max} \sim 10^4$ to explain the observed flux ratios in the NIR and X-ray. In contrast, in one-zone models, the SSC–SSC scenario requires particle densities 10^3 higher than typically inferred for the ambient accretion flow.

Appendix D: Analytical formulation of the non-thermal electron distributions

We considered nonthermal electron distributions for the modeling of the flare SED in this paper. These are either in the form of a plain power law or a broken power law. In this section, we describe the analytical form of these distributions.

– The formulation of the power-law electron distribution is given in Equation D.1. In that equation, n_e is the electron density, p is the power-law index, and γ_{min} and γ_{max} are the low- and high-energy limits of the electron population,

$$\frac{dn_{\mathrm{pl}}}{d\gamma} = n_e \times \begin{cases} N_{\mathrm{pl}}\gamma^{-p}, & \text{if } \gamma_{min} \le \gamma \le \gamma_{max} \\ 0, & \text{otherwise,} \end{cases} \tag{D.1}$$

where N_{pl} is the normalization of the distribution,

$$N_{\mathrm{pl}} = \frac{p-1}{{\gamma_{min}}^{1-p} - {\gamma_{max}}^{1-p}}. \tag{D.2}$$

– We provide a generic formulation of a broken power-law electron distribution in Equation D.3. Since we consider synchrotron cooling as the origin of the break at γ_b, we enforced $p_2 = p_1 + 1$. For readability, we used the notation p in the main text for all power-law indices. In the case of cooled synchrotron spectra it corresponds to p_1,

$$\frac{dn_{\mathrm{bpl}}}{d\gamma} = n_e \times \begin{cases} N_{\mathrm{bpl}}\gamma^{-p_1}, & \text{if } \gamma_{min} \le \gamma \le \gamma_b \\ N_{\mathrm{bpl}}\gamma^{-p_2}\gamma_b^{p_2-p_1}, & \text{if } \gamma_b < \gamma \le \gamma_{max} \\ 0, & \text{otherwise,} \end{cases} \tag{D.3}$$

where N_{bpl} is the normalization of the distribution,

$$N_{\mathrm{bpl}} = \left[\left(\frac{\gamma_{min}^{1-p_1} - \gamma_b^{1-p_1}}{p_1 - 1}\right) + (\gamma_b)^{p_2-p_1}\left(\frac{\gamma_b^{1-p_2} - \gamma_{max}^{1-p_2}}{p_2 - 1}\right)\right]^{-1}. \tag{D.4}$$

Considering synchrotron cooling in the presence of particle escape as the origin for the broken power-law distribution, a sharp cooling break in the electron distribution is not physical. However, the exact determination of the spectral shape is beyond the scope of this work. Furthermore, our observational data does not provide useful constraints on the cooling break itself, and thus the determination of the proper shape of the break is not required. For simplicity, we use the form given in Equation D.3.

In above formulas, the electron distributions are truncated at both γ_{min} and γ_{max}. As a more physical alternative, we use an exponential cutoff instead of a sharp truncation at γ_{max},

$$\frac{dn_{\mathrm{expc}}}{d\gamma} = \begin{cases} (dn/d\gamma)\exp(-\gamma/\gamma_{max}), & \text{if } \gamma_{min} \le \gamma \le 10 \times \gamma_{max} \\ 0, & \text{otherwise,} \end{cases} \tag{D.5}$$

that is, we simply smooth the high-energy cutoff of the original electron distributions with an exponential function. The high energy limit is extended from γ_{max} to $10 \times \gamma_{max}$.